Friedrich-Schiller-Universität Jena
Physikalisch-Astronomische Fakultät

BACHELORARBEIT
im Studiengang *Physik (B. Sc.)*

Global Analytic Approximation to the Wilson-Fisher Fixed Point Potential

Lennart Dabelow

5. Februar 2015

---

1. Gutachter: Prof. Dr. Holger Gies
2. Gutachter: Dr. Omar Zanusso

Friedrich-Schiller-Universität Jena
Physikalische-Astronomische Fakultät · Theoretisch-Physikalisches Institut (TPI)

Bachelorarbeit von Lennart Dabelow
im Studiengang *Physik (B. Sc.)*
Wintersemester 2014/15

Erstgutachter: Prof. Dr. Holger Gies / TPI
Zweitgutachter: Dr. Omar Zanusso / TPI

Eingereicht am: 05.02.2015

Global Analytic Approximation to the Wilson-Fisher Fixed Point Potential

Abstract

We investigate the fixed point equation for the effective average action of the functional renormalization group in the local potential approximation. First, we derive approximate analytic solutions to the average potential in the $\mathbb{Z}_2$ model in $d = 3$ Euclidean dimensions in terms of series expansions and rational functions. Thereafter, we perturb the potential around the fixed point and determine critical properties of theories built around it.

After a quick review of the origin of the flow equation, we compute Taylor-like series up to order 2000 in the limits of vanishing and infinite values of the $\mathbb{Z}_2$ invariant classical field. For the small field case, we uncover a peculiar regularity of the signs of its coefficients and, by the use of Padé approximants, find evidence that suggests a relation to branch points of the potential in the complex plane.

The large field series shows excellent convergence, and we are able to join both series in a connecting interval. We then compute Padé approximants to the large field series, which allows us to specify a finite approximation on the whole physical domain and reproduces features of the small field series. A slightly modified branch point structure is noted.

We refine the global approximation by incorporating information from both series into a single rational function. This way, we are able to specify the fixed point potential up to a total (integrated) deviation of less than 2×10^{-8}. We also monitor the transition of the branch point structure as suggested by the two limiting cases.

Finally, we compute critical exponents from the various approximation schemes. This is first done by determinating the eigenvalues of the stability matrix of the series expansions. For the small field series, our results agree well with literature values. For the large field series, the stability matrix is degenerated and the method fails. By means of the Padé-Hankel method, we are able to obtain a spectrum, but it appears to be distorted. In addition, we provide a method to calculate critical exponents from Padé coupling constants by virtue of a transformation of β functions and show that the information of the composing parts is retained.

Lennart Dabelow
Matrikelnr.: 128 530
Johann-Griesbach-Str. 7
07743 Jena
lennart.dabelow@uni-jena.de

Ich versichere, vorliegende Bachelorarbeit selbständig und nur unter Verwendung der angegebenen Hilfsmittel und Quellen verfasst zu haben. Die Arbeit ist nicht anderweitig als Prüfungsleistung verwendet und nicht in englischer oder einer anderen Sprache veröffentlicht worden.

Von meiner Seite bestehen keine Einwände, die Arbeit zur öffentlichen Einsicht freizugeben.

Jena, 05.02.2015

Lennart Dabelow

Contents

Introduction

As of today, the most precise theories linking microscopic and macroscopic physics are quantum field theories. Despite their tremendous success, actual calculations within this framework turn out to be rather tedious and cumbersome, and several difficulties have to be overcome. The most prevailing of these subtleties, which also deferred the acceptance of quantum electrodynamics as the first experimentally confirmed quantum field theory, is the understanding of how to deal with apparent divergencies emerging from the formulae.

Historically, this problem was attacked by means of *perturbative renormalization* developed by Feynman, Schwinger, and Tomonaga in order to obtain finite predictions from the theory of quantum electrodynamics [1–4]. This idea is based upon a perturbative expansion of the correlation functions in the coupling constants, leading to the notion of Feynman diagrams and loop expansions. Divergencies in the couplings like masses and charges are canceled by so-called counterterms which are defined such that the theory is left with the experimentally determined values of these couplings. The *renormalization group* as introduced by Wilson [5] and comprehensively extended to the formalism employed here by Polchinski, Wetterich, Morris, and others [6–8] generalizes the concept of renormalized field theories in a nonperturbative way. It thereby naturally bridges between quantum and statistical field theory.

The basic and rather simple idea is that physics is generically scale-dependent: We use different models to describe phenomena at different scales. For example, the concept of spin is used to describe magnetic interactions at the atomic scale, whereas the macroscopic magnetization is the relevant quantity for statistical ensembles. Of course, a fundamental task of theoretical physics is to link the microscopic concepts such as the spin to their effective counterparts at a scale accessible to experiment, e.g. the magnetization.

The renormalization group transfers this principle to field theory. Starting from a microscopic, "bare" action defined at some small-distance/high-energy scale, we wish to find an effective theory described by an effective action, valid at some low-energy scale. Within the framework of the *exact* or *functional renormalization group*, this is achieved by continuously lowering the scale and averaging over fluctuations at higher energies.

The mathematical space in which this process is carried out is the space of all possible theories (with some restrictions to dimensionality and degrees of freedom). The aim of our analysis is then to single out the physically realized theories among them. To do so, fixed points are particularly interesting because they represent points of attraction along certain directions in theory space. As the scale is lowered and the effective action "flows" through the space of all theories, it inevitably approaches a fixed point along these directions. However, the fixed point may be repulsive in some other direction, and the theory will thus drift away from it, unless the corresponding parameter of the trajectory is fine-tuned to its fixed point value. In this way, theories align along these repulsive directions, and the number of such directions is related to the system's degrees of freedom.

In this thesis, we shall study a rather specific class of quantum field theories, namely the $O(1)$ or $\mathbb{Z}_2$ symmetric real scalar field in three dimensions, which is related to the Ising model known from statistical physics. It is a remarkable result confirmed both theoretically and experimentally that quite distinct physical systems show the same behavior in the low-energy limit. This can be understood by noting that the field theoretic structure of these systems is similar, and hence their macroscopic properties are controlled by the same fixed points. The principle of *universality* states that the number of critical points and the associated critical exponents are essentially determined by the number of space-time dimensions and the symmetry group of the order parameter, though other criteria may be added [9, p. 22].

Besides the trivial Gaussian fixed point corresponding to a non-interacting theory, the model studied here possesses one more fixed point called the *Wilson-Fisher fixed point*. Our goal is to derive a global analytic approximation to the *effective potential* as part of the effective action at the fixed point. While this is merely a theoretical construct, generally depending on the averaging procedure, we shall thereafter extract physical information in the form of critical exponents that can in principle be measured by experiment.

Our roadmap is as follows: First, we shall quickly derive the differential equation characterizing the flow of the effective potential. A first attempt to solve the associated fixed point equation will be made in terms of *series expansions* in the limit of small and large field, respectively. We shall extensively study the converging behavior and peculiarities of these series. A prominent tool will be the method of *Padé approximants*. These will also be used thereafter to combine the asymptotic information from both series into a single approximative expression of the potential in its entire domain. Finally, we shall investigate how much of the critical information is stored in the respective series expansions and preserved by our global approximations.

Throughout this work, we shall focus on an analytic approach to the Wilson-Fisher fixed point. Although the topic is most commonly studied by numerical methods, some analytic approximations have been discussed, e.g. [10–13]. Aspects of the use of the Padé method in the context of critical phenomena and renormalization group equations have been covered in [14, 15]. Nevertheless, we hope to provide at least a very few new insights into the problem.

1 Renormalization Group Flow for Scalar Fields

As a start, we would like to give a quick derivation of the simple renormalization group equations needed here. It will basically follow along the lines of [16–20]. We restrict our discussion to a single real-valued scalar field $\chi = \chi(x)$. Also, we are working in d-dimensional Euclidean space where we shall eventually set $d = 3$, and natural units ($\hbar = c = 1$) are understood.

1.1 Basic Quantum Field Theory

Let us collect some basics of quantum field theory in order to clarify notation and to set the stage for the subsequent derivation. In general, all physical information of a system described by an action S is encoded in the *n-point correlation functions* [17]. In the path integral formalism, these read

$$\langle \chi(x_1) \cdots \chi(x_n) \rangle = \frac{\int \mathcal{D}\chi \, \chi(x_1) \cdots \chi(x_n) \, \mathrm{e}^{-S[\chi]}}{\int \mathcal{D}\chi \, \mathrm{e}^{-S[\chi]}} \,, \tag{1.1}$$

where $\langle \cdots \rangle$ denotes the vacuum expectation value. Introducing a source $J(x)$ as an auxiliary function, all correlation functions can be obtained from the *generating functional*

$$Z[J] := \int \mathcal{D}\chi \, \mathrm{e}^{-S[\chi] + \int \mathrm{d}^d x \, J(x)\chi(x)} \tag{1.2}$$

by functional differentiation:

$$\langle \chi(x_1) \cdots \chi(x_n) \rangle = \frac{1}{Z[0]} \frac{\delta^n Z[J]}{\delta J(x_1) \cdots \delta J(x_n)} \bigg|_{J=0} \,. \tag{1.3}$$

In classical field theory, the phase space trajectory of the system's configuration is determined by the requirement that the action be stationary, and the field expectation value may be computed as the configuration that minimizes the potential energy. Unfortunately, quantum fluctuations resulting from perturbative loop diagrams generally demolish this classical picture [16, p. 364]. Nevertheless, there is still a potential called the *effective action* Γ which is minimized by the vacuum expectation value $\langle \chi \rangle$.

In order to find this quantity, we introduce the *Schwinger functional* $W[J] := \ln Z[J]$ comparable to the free energy in statistical physics. It can be shown that W generates the *connected correlation functions* [17]. In particular,

$$\frac{\delta W[J]}{\delta J(x)} = \frac{1}{Z[J]} \int \mathcal{D}\chi \, \chi(x) \mathrm{e}^{-S[\chi] + \int \mathrm{d}^d x' \, J(x')\chi(x')} = \langle \chi \rangle_J \,. \tag{1.4}$$

For $J = 0$, this is the vacuum expectation value and thus the variable to minimize our new potential. Therefore, we define $\phi := \langle \chi \rangle_J$, also called the *classical field* [16, p. 366]. In a sense, this is a more physical variable because any measurement we can carry out on a system has averaging character. The change of the independent variable is mediated by a Legendre transformation, leading precisely to the definition of the effective action:

$$\Gamma[\phi] := \int \mathrm{d}^d x \, J(x)\phi(x) - W[J] \,, \tag{1.5}$$

where J is considered to be a function of ϕ obtained by inverting (1.4). If W is not strictly convex, the supremum over J is understood. As a general property, the Legendre transform is its own inverse and we have

$$\frac{\delta \Gamma[\phi]}{\delta \phi(x)} = J(x) \,, \tag{1.6}$$

so that the vacuum configuration $\phi_0 = \langle\chi\rangle$ obtained at $J = 0$ is indeed a minimum (or at least a stationary point) of Γ. Furthermore, it is found that the effective action Γ is the generating functional of the one-particle irreducible correlation functions [16, p. 383]. It is the potential where all quantum fluctuations have been integrated out, such that we are left with an effective theory.

Unfortunately, the direct calculation of Γ is not easier at all than calculating the generating functional Z in the first place, so there is no immediate advantage from a practical point of view. Nevertheless, the *renormalization group* (RG) provides step-by-step instructions to interpolate between the microscopic action and the effective theory.

1.2 Functional Renormalization Group and Flow Equation

The idea of the *functional* or *exact renormalization group* is to continuously transform from the bare action S to the effective action Γ by successively integrating-out quantum fluctuations at intermediate energy scales. In other words, one starts with the bare (classical) action S defined at some microscopic length scale Λ^{-1} (e.g. the Planck scale, lattice spacing) corresponding to the high-energy limit. This energy or momentum scale is then lowered in infinitesimal steps such that all high-energy fluctuations are averaged over.

For this, we introduce a new generating functional depending on some momentum scale k. Namely, we shall define the *(effective) average action* $\Gamma_k[\phi]$ in such a way that it is an effective action which only includes fluctuations with momenta $p \gtrsim k$ [18]. The scale-dependence of Γ_k is then bounded by the conditions $\Gamma_{k\to\Lambda} = S$ (all fluctuations present) and $\Gamma_{k\to 0} = \Gamma$ (all fluctuations integrated-out, the full effective theory). Consequently, Γ_k depends on the modes of the field that have already been integrated out [19], i.e. ϕ is to be the average value of the field χ at momenta $p \gtrsim k$. To implement the screening of low-energy modes, we add an infrared cut-off to the generating functional:

$$Z_k[J] := \int \mathcal{D}\chi \, \mathrm{e}^{-S[\chi]-\Delta S_k[\chi]+\int \mathrm{d}^d x \, J(x)\chi(x)} \tag{1.7}$$

with

$$\Delta S_k[\chi] := \int \frac{\mathrm{d}^d p}{(2\pi)^d} \chi(-p) R_k(p^2) \chi(p) \tag{1.8}$$

being a momentum dependent mass term which effectively suppresses the modes with $p \lesssim k$ [19]. We may also express it as a position space integral,

$$\Delta S_k[\chi] = \int \mathrm{d}^d x \, \mathrm{d}^d y \, \chi(x) R_k(x,y) \chi(y) \,, \tag{1.9}$$

where $R_k(x,y) = R_k(-\partial^2)\,\delta(x-y)$ denotes the Fourier transform of the momentum space *regulator* $R_k(p,p') = 2\pi\delta(p+p')R_k(p^2)$. The interpolating Schwinger functional is obtained straightforwardly as $W_k = \ln Z_k$, and we define the classical field $\phi := \delta W_k/\delta J$ as before. The regulator R_k is required to have the following properties in order to mediate the above mentioned interpolation [17]:

$$\lim_{p^2/k^2\to 0} R_k(p^2) = 0+ \qquad \text{and} \qquad \lim_{k\to\Lambda} R_k(p^2) \to \infty \,. \tag{1.10}$$

The first condition ensures $Z_{k\to 0} = Z$ and thus $\Gamma_{k\to 0} = \Gamma$ as we shall see from the following definition. The second condition takes care of the high-energy limit, but in order to arrive at the correct boundary value, we define Γ_k by a slightly modified Legendre transform [17, 19]:

$$\Gamma_k[\phi] := \int \mathrm{d}^d x \, J(x)\phi(x) - W[J] - \Delta S_k[\phi] \,. \tag{1.11}$$

Computing an integral representation of Γ_k, it can be shown that this definition indeed satisfies the condition $\Gamma_{k\to\Lambda} \to S$, at least in the case of a sharp high-energy cut-off Λ [17, 18]. Apart from conditions (1.10), the choice of a regulator function R_k is rather free. The precise form of the regulator

has a significant impact on the average action Γ_k, but at least in theory it cannot alter any physical quantities in general and the effective action Γ in particular. However, due to the fact that we will eventually have to make approximations, certain regulator functions have shown to be more suitable than others [21].

Note that due to the modified definiton of Γ_k, the source J is now obtained from the average action as

$$J(x) = \frac{\delta \Gamma_k[J]}{\delta \phi(x)} + \int \mathrm{d}^d y \, R_k(x,y)\phi(y)\,, \tag{1.12}$$

and as a funtional of each other, both J and ϕ are now scale-dependent.

Our aim is to find the dependence of the average action Γ_k on the scale k. It is common and convenient to introduce a dimensionless scale parameter $t := \ln(k/\Lambda)$, the so-called *renormalization group time*, which runs "backwards" from the bare scale at $t = 0$ to the effective scale at $t = -\infty$. We now investigate how the average action changes with the scale by taking the partial derivative $\partial_t \equiv k\,\partial_k$ of (1.11):

$$\partial_t \Gamma_k[\phi] = \int \mathrm{d}^d x \frac{\partial J(x)}{\partial t}\phi(x) - \frac{\partial W_k}{\partial t}[J] - \int \mathrm{d}^d x \frac{\delta W_k[J]}{\delta J(x)} \frac{\partial J(x)}{\partial t} - \frac{\partial \Delta S_k}{\partial t}[\phi]\,.$$

The dependece of W_k upon k is two-fold: On the one hand, there is the parametric dependence via the regulator term in (1.7), which is meant by $\partial W_k/\partial t$. On the other hand, there is the implicit dependence via J according to (1.12). Since $\delta W_k/\delta J = \phi$, the first and third term cancel, leading to

$$\partial_t \Gamma_k[\phi] = -\frac{\partial W_k}{\partial t}[J] - \frac{1}{2}\int \mathrm{d}^d x \, \mathrm{d}^d y \, \phi(x) \frac{\partial R_k}{\partial t}(x,y)\,\phi(y)\,. \tag{1.13}$$

The flow of the Schwinger functional is given by

$$\begin{aligned}
\partial_t W_k[J] &= -\frac{1}{Z_k[J]} \int \mathcal{D}\chi \, \frac{\partial \Delta S_k}{\partial t}[\chi]\, \mathrm{e}^{-S[\chi] + \int J\chi - \Delta S_k[\chi]} \\
&= -\frac{1}{Z_k[J]} \int \mathcal{D}\chi \, \frac{1}{2}\int \mathrm{d}^d x \, \mathrm{d}^d y \, \frac{\partial R_k}{\partial t}\chi(x)\chi(y)\, \mathrm{e}^{-S[\chi] + \int J\chi - \Delta S_k[\chi]} \\
&= -\frac{1}{2Z_k[J]} \int \mathrm{d}^d x \, \mathrm{d}^d y \, \frac{\partial R_k}{\partial t} \frac{\delta^2}{\delta J(x)\delta J(y)} \int \mathcal{D}\chi \, \mathrm{e}^{-S[\chi] + \int J\chi - \Delta S_k[\chi]} \\
&= -\frac{1}{2}\int \mathrm{d}^d x \, \mathrm{d}^d y \, \frac{\partial R_k}{\partial t} \left\langle \chi(x)\chi(y) \right\rangle_k \,.
\end{aligned}$$

Using

$$\left\langle \chi(x)\chi(y) \right\rangle_k = \frac{\delta^2 W_k[J]}{\delta J(x)\delta J(y)} + \frac{\delta W_k[J]}{\delta J(x)} \frac{\delta W_k[J]}{\delta J(y)} = \frac{\delta^2 W_k[J]}{\delta J(x)\delta J(y)} + \phi(x)\phi(y)$$

and plugging everything into (1.13), we obtain

$$\partial_t \Gamma_k[\phi] = \frac{1}{2}\int \mathrm{d}^d x \, \mathrm{d}^d y \, \frac{\partial R_k}{\partial t} \frac{\delta^2 W_k[J]}{\delta J(x)\delta J(y)}\,. \tag{1.14}$$

In order to express this in terms of Γ_k only, we write

$$\frac{\delta^2 W_k[J]}{\delta J(x)\delta J(y)} = \frac{\delta \phi(y)}{\delta J(x)} = \left(\frac{\delta J(x)}{\delta \phi(y)}\right)^{-1} \overset{(1.12)}{=} \left(\frac{\delta^2 \Gamma_k[\phi]}{\delta\phi(x)\delta\phi(y)} + R_k(x,y)\right)^{-1}\,.$$

Hence we obtain the flow equation for the effective average action:

$$\partial_t \Gamma_k[\phi] = \frac{1}{2} \int \mathrm{d}^d x \, \mathrm{d}^d y \, \frac{\partial R_k}{\partial t} \left(\frac{\delta^2 \Gamma_k[\phi]}{\delta\phi(x)\delta\phi(y)} + R_k(x,y) \right)^{-1} . \tag{1.15}$$

Of course, the integral may be performed in momentum space, too; we can write (1.15) basis-independently in operator form,

$$\partial_t \Gamma_k = \frac{1}{2} \operatorname{Tr} \left[\left(\Gamma_k^{(2)} + R_k \right)^{-1} \partial_t R_k \right] . \tag{1.16}$$

In order to solve the theory, one has to solve this first-order nonlinear functional differential equation for Γ_k with the initial condition $\Gamma_\Lambda \simeq S$. In general, no exact solution to this problem is known, and approximations regarding the form of the average action are necessary.

1.3 Local Potential Approximation

We shall employ the so-called *local potential approximation* (LPA) [10, 22–25], assuming the average action to be of the form

$$\Gamma_k[\phi] = \int \mathrm{d}^d x \left[\frac{1}{2} \partial_\mu \phi \partial^\mu \phi + U_k(\phi) \right] , \tag{1.17}$$

i.e. we only consider the leading order of the derivative expansion. Also, we do not include field-strength renormalization, thus setting the anomalous dimension to zero. In general, this is a dramatic simplification. In the case of a single field in three dimensions studied here, higher order corrections are relatively small [26]. Evaluating

$$\frac{\delta^2 \Gamma_k[\phi]}{\delta\phi(x)\delta\phi(x')} = \left[-\partial^2 + U_k''(\phi(x)) \right] \delta(x - x')$$

and using the fact that in position space $R_k(x,x') = \delta(x-x') R_k(-\partial^2)$ where $R_k(p^2)$ denotes the regulator in momentum space, we define $\tilde{R}_k(p^2) = p^2 + R_k(p^2)$, such that the flow equation (1.16) can be written

$$\partial_t \Gamma_k[\phi] = \frac{1}{2} \operatorname{Tr} \left[\frac{\partial_t \tilde{R}_k}{\tilde{R}_k + U_k''(\phi)} \right] = \frac{1}{2} \int \frac{\mathrm{d}^d p}{(2\pi)^d} \frac{\partial_t \tilde{R}_k(p^2)}{\tilde{R}_k(p^2) + U_k''(\phi)} .$$

Since we are primarily interested in the effective potential, it is sufficient to restrict ourselves to the case of a uniform field $\phi = \text{const}$. This way we assume the vacuum configuration that minimizes Γ to be invariant under Poincaré transformations [16, p. 367]. The average action is then proportional to the average potential, $\Gamma_k = \Omega U_k$, where $\Omega = \int \mathrm{d}^d x$ denotes the volume of the system. Absorbing this volume, the flow of the effective average action reduces to a flow equation for the effective average potential:

$$\partial_t U_k(\phi) = \int \frac{\mathrm{d}^d p}{(2\pi)^d} \frac{\partial_t \tilde{R}_k(p^2)}{\tilde{R}_k(p^2) + U_k''(\phi)} . \tag{1.18}$$

Throughout this thesis, we will be using the optimized regulator

$$R_k(p^2) = (k^2 - p^2) \Theta(k^2 - p^2) , \tag{1.19}$$

which is known to yield the maximum radius of convergence of a series expansion in the LPA [21]. From this choice, we find $\partial_t \tilde{R}_k(p^2) = \partial_t R_k(p^2) = 2k^2 \Theta(k^2 - p^2)$. Plugging this into (1.18) and

performing the angular integration results in

$$\begin{aligned}\partial_t U_k(\phi) &= \frac{S_d}{(2\pi)^d}\int_0^\infty \mathrm{d}p\, p^{d-1}\frac{2k^2\Theta(k^2-p^2)}{p^2+(k^2-p^2)\Theta(k^2-p^2)+U_k''(\phi)}\\ &= \frac{S_d}{(2\pi)^d}\int_0^k \mathrm{d}p\, p^{d-1}\frac{2k^2}{k^2+U_k''(\phi)}\,,\end{aligned}$$

where $S_d = 2\pi^{d/2}/\Gamma(\frac{d}{2})$ denotes the surface of the d-dimensional unit sphere. Consequently,

$$\partial_t U_k(\phi) = k^d\left[\frac{2S_d}{(2\pi)^d d}\right]\frac{1}{1+k^{-2}U_k''(\phi)}\,. \tag{1.20}$$

Since we will be looking for a scale-invariant fixed point, we switch to dimensionless variables, which is to say that the averaging procedure is accompanied by a rescaling to the intrinsic scale in order that quantities at different scales are comparable. Therefore, we express the field and effective average potential as

$$\tilde\phi := k^{\frac{2-d}{2}}\phi \qquad \text{and} \qquad u_k(\tilde\phi) := k^{-d}U_k(\phi) = k^{-d}U_k(k^{\frac{d-2}{2}}\tilde\phi)\,, \tag{1.21}$$

respectively. The flow of the dimensionless potential is then given by

$$\partial_t u_k(\tilde\phi) = -d\,k^{-d}\,U_k(\phi) + \frac{d-2}{2}\,\tilde\phi\,k^{-\frac{d+2}{2}}\,U_k'(\phi) + k^{-d}\,\partial_t U_k(\phi)\,.$$

Substituting (1.20) and using $u_k'(\tilde\phi) = k^{-\frac{d+2}{2}}U_k'(\phi)$, $u_k''(\tilde\phi) = k^{-2}U_k''(\phi)$, we obtain

$$\partial_t u_k(\tilde\phi) = -d\,u_k(\tilde\phi) + \frac{d-2}{2}\,\tilde\phi\,u_k'(\tilde\phi) + \left[\frac{2S_d}{(2\pi)^d d}\right]\frac{1}{1+u_k''(\tilde\phi)}\,, \tag{1.22}$$

the flow equation for the dimensionless effective average potential. Its full RG transformation thus consists of a *scaling part*, namely the first two terms on the right-hand side, and an *averaging* or *coarse-graining part*, the last term of (1.22).

Finally, we require $\mathbb{Z}_2$ or $O(1)$ symmetry, i.e. the potential is to be invariant under the transformation $\tilde\phi \mapsto -\tilde\phi$, which is the one-dimensional analog to an invariance under orthogonal transformations $O(N)$ and ensures that the potential is asymptotically convex. Hence assume $u_k(\tilde\phi) = v_k(\rho)$, where $\rho = \frac{1}{2}\tilde\phi^2$. Consequently, $u_k''(\tilde\phi) = v_k'(\rho) + 2\rho v_k''(\rho)$. This leads to the flow equation for the $\mathbb{Z}_2$-invariant potential:

$$\partial_t v_k = -dv_k + (d-2)\rho v_k' + \left[\frac{2S_d}{(2\pi)^d d}\right]\frac{1}{1+v_k'+2\rho v_k''}\,. \tag{1.23}$$

In search of a fixed point, we shall set $\partial_t v_k = 0$, thus obtaining a nonlinear ordinary differential equation for v. It should be noted that, although this equation is of second order, there is only one free parameter left due to the fact that we have lost one degree of freedom when assuming $\mathbb{Z}_2$ invariance. This will become clear later when we expand v in powers of ρ. However, it can already be seen in (1.23) where the second derivative of the average potential is multiplied by the field, effectively restoring one order in a series expansion as opposed to (1.22) where the second derivative occurs nakedly.

In the following, we will primarily be working in $d = 3$ dimensions, hence

$$\partial_t v_k = -3v_k + \rho v_k' + \frac{1}{6\pi^2}\frac{1}{1+v_k'+2\rho v_k''} \tag{1.24}$$

is the flow equation of interest.

2 Wilson-Fisher Fixed Point Solution

As it has been mentioned in the introduction, fixed points of the flow equation are of special interest because they represent points of attraction at least along certain directions in theory space and thus correspond to physically realized theories. Starting with an arbitrary initial condition at some high-energy scale Λ, the theory will naturally evolve towards a fixed point along these directions as the scale is lowered. Therefore, the number of repulsive directions determines the theory's degrees of freedom: these are the parameters that must be fine-tuned carefully in order to arrive at the correct effective theory. This will be examined in greater depth in Section 3.

In any space-time dimension, the free theory where the action is of the form $S = \int \mathrm{d}^d x \, (\partial\phi)^2$ is a fixed point of the renormalization group transformation, called the Gaussian fixed point [16, 27]. For high-dimensional systems, the Gaussian fixed point is stable and theories can be constructed as perturbative expansions of the free theory. For $d < 4$, however, the Gaussian fixed point becomes unstable, and new fixed points emerge that determine the low-energy limit [16, pp. 402-403]. In $d = 3$ dimensions and within our approximation scheme, we will find one such extra fixed point, namely the Wilson-Fisher fixed point. In the language of statistical physics, it describes a second-order phase transition, i.e. the theory is on the edge between the symmetric and spontaneously broken regimes [10].

Setting $\partial_t v_k = 0$ in (1.24) we arrive at the 3-dimensional fixed point equation for the average potential,

$$3v - \rho v' = \frac{1}{6\pi^2} \frac{1}{1 + v' + 2\rho v''} \,. \tag{2.1}$$

No exact solution of (2.1) is known, and in order to find an approximation of the fixed point potential we shall discuss two limiting cases first, namely $\rho \to 0$ and $\rho \to \infty$.

2.1 Small Field Asymptotics

2.1.1 Series Expansion

In order to obtain an approximate analytical solution of (2.1) for $\rho \ll 1$, we expand the effective potential in a power series around the origin,

$$v(\rho) = \sum_{n=0}^{\infty} c_n \rho^n \,. \tag{2.2}$$

Thus we can express the flow of the effective potential v in terms of the evolution of the coupling constants c_n. Plugging the ansatz into the right-hand side of (1.24), we find

$$\begin{aligned} \partial_t v &= \left[-3c_0 + \frac{1}{6\pi^2(1+c_1)} \right] + \rho \left[-2c_1 - \frac{c_2}{\pi^2(1+c_1)^2} \right] \\ &\quad + \rho^2 \left[-c_2 + \frac{1}{6\pi^2} \left(\frac{36c_2^2}{(1+c_1)^3} - \frac{15c_3}{(1+c_1)^2} \right) \right] + \dots \\ &=: \sum_n \beta_n(\boldsymbol{c}) \rho^n \,, \end{aligned} \tag{2.3}$$

where we introduced the β functions β_0, β_1, ... by collecting powers of ρ. These govern the evolution of the coupling constants as can be seen by substituting (2.2) into the left-hand side of (1.24):

$$\partial_t c_n = \beta_n(\boldsymbol{c}) \,. \tag{2.4}$$

Note that the derivative does not act on the field ρ; the k dependence of ρ has already been accounted for when switching to dimensionless variables in (1.21).

Tab. 1: First coefficients in a Taylor expansion of the fixed point potential for small field

c_0	$1/18\pi^2(1+\lambda)$
c_1	λ
c_2	$-2\pi^2\lambda(1+\lambda)$
c_3	$\frac{4}{5}\pi^4\lambda(1+\lambda)^3(1+13\lambda)$
c_4	$-\frac{72}{7}\pi^6\lambda^2(1+\lambda)^4(1+7\lambda)$
c_5	$\frac{32}{35}\pi^8\lambda^2(1+\lambda)^5(2+121\lambda+623\lambda^2)$
c_6	$-\frac{32}{385}\pi^{10}\lambda^2(1+\lambda)^6(-4+429\lambda+13362\lambda^2+58289\lambda^3)$
c_7	$\frac{2304}{35035}\pi^{12}\lambda^2(1+\lambda)^7(1-153\lambda+6114\lambda^2+160345\lambda^3+653037\lambda^4)$
c_8	$-\frac{384}{175175}\pi^{14}\lambda^2(1+\lambda)^8(-6-544\lambda-142327\lambda^2+994146\lambda^3+42524975\lambda^4+177605120\lambda^5)$

At the fixed point, $\partial_t v = 0$, and thus we are left with a set of $n_{\text{trunc}}+1$ coupled algebraic equations for the coefficients c_0, c_1, ..., namely

$$\beta_n(\boldsymbol{c}) = 0 \quad \text{for all } n = 0, \dots, n_{\text{trunc}}\,. \tag{2.5}$$

It now becomes manifest that there is one free parameter left because in general, β_n depends on all couplings $c_0, \dots, c_{n+1}$. We choose this free parameter to be the mass term $c_1 := \lambda$.

For computational reasons, however, it is advantageous to work with (2.1) directly. Substituting (2.2), multiplying by the right-hand side's denominator and collecting powers of ρ, we are lead to a recurrence relation of the form

$$\begin{aligned}
c_0 &= \frac{1}{18\pi^2}\frac{1}{1+\lambda}\,,\\
c_1 &= \lambda\,,\\
c_2 &= -2\pi^2\lambda(1+\lambda)^2\,,\\
c_{n+3} &= \frac{1}{(n+3)(6n+15)c_0}\Bigg[(n-1-(2n+4)c_1)\,c_{n+2}\\
&\qquad + \sum_{j=0}^{n}\frac{1}{j!}\left((j+1)(n-j-1)c_{j+1}c_{n-j+2} + 2(j+2)(j+1)(n-j-2)c_{j+2}c_{n-j+1}\right)\Bigg]\,.
\end{aligned} \tag{2.6}$$

The first few coefficients in terms of the parameter λ are collected in Table 1.

2.1.2 Convergence Behavior and the Parameter λ

The coupling constant λ in the above expansion of the effective potential is in fact not arbitrary. The free parameter appears as a side effect of truncation. The standard procedure to choose λ is to require that $c_{n_{\text{trunc}}+1}$ vanish, but this choice is usually not unique and depends on the truncation. We want to fix λ in such a way that the obtained power series reaches its maximum radius of convergence [26,28]. The radius of convergence of a series like (2.2) is given by [29, p. 75]

$$\rho_c = 1/\limsup_{n\to\infty}\sqrt[n]{|c_n|}\,. \tag{2.7}$$

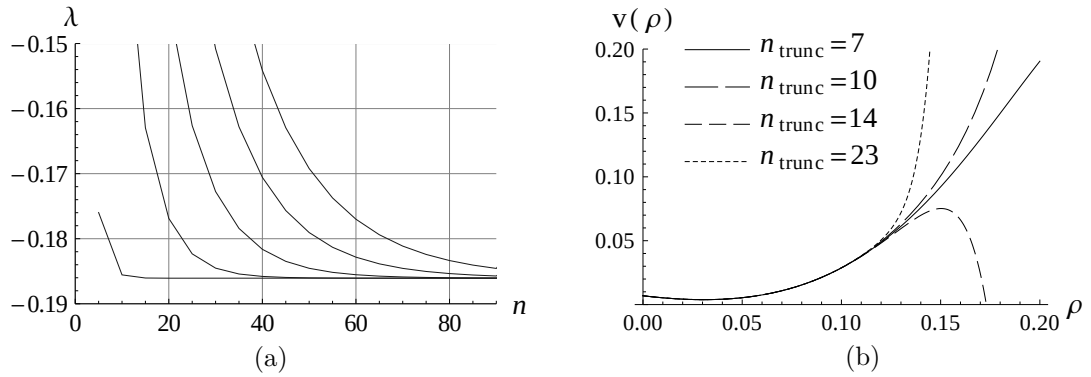

Fig. 1: (a) First five roots of the coefficients c_n as a function of n. Only roots in the interval $(-1, 0)$ are considered, and for each c_n the roots are enumerated from left to right. Thus the leftmost curve describes the evolution of the first root, next the evolution of the second, and so on. The roots converge to $\lambda_\star = -0.186\,064\,2...$ as n is increased; (b) examples plots of the small field expansion for different truncations n_{trunc} with $\lambda = -0.186\,064\,2$.

From Table 1 we see that the coefficients c_n are polynomials in λ. Therefore, in order to maximize ρ_c, it seems reasonable to look for common roots of the c_n. There are two trivial choices, $\lambda = -1$ and $\lambda = 0$, both of which reduce to constant potential. The former is a mere peculiarity of the equation and is not related to a scaling solution [30]: $v = c_0 = \infty$ does not satisfy (2.1). By contrast, the latter, $\lambda = 0$, corresponds to the theory's Gaussian fixed point seeing as only the derivative term in the effective action (1.17) survives.

Since the Wilson-Fisher fixed point is related to a second-order phase transition, we want $u''(0) < 0$, so that the potential is concave at the origin and $\lim_{k\to 0} U_k''(0) \to 0-$. Carried over to v, we therefore need $\lambda_\star < 0$ for the parameter $\lambda_\star$ describing the Wilson-Fisher fixed point. In view of the divergence of v as $\lambda \to -1$, it is expected to lie somewhere in the interval $(-1, 0)$ in order to allow for a smooth transition from the Gaussian to the Wilson-Fisher fixed point.

Analyzing the dependence of the roots of the c_n in $(-1, 0)$ upon the order n, we first find that all of them roots lie in the interval $(-0.2, 0)$. Furthermore, they tend to drift to the left towards the lower bound of this interval with increasing n. Sorting and enumerating the roots from left to right, we can study their "evolution" as a function of the order n. This reveals indeed a converging behavior, as can be seen from Figure 1(a). As the order is increased, the roots move to the bottom to finally merge at $\lambda_\star = -0.186\,064\,2...$, which we shall use as the defining value of the Wilson-Fisher fixed point potential as a start. This is in accordance with [26, 28, 31].

Having fixed the value of λ, we turn our attention to the converging behavior of the series expansion itself. A few examples of the truncated series are plotted in Figure 1(b). Bearing in mind the definiton of the radius of convergence (2.7), we take $1/\sqrt[n]{|c_n|}$ as an estimate of ρ_c. From Figure 2(a), $\rho_c \approx 0.1$ seems to be reasonable considering the first 200 coefficients. Looking at the absolute values of the coefficients themselves, depicted in Figure 2(b), we find an approximately exponential growth of the c_n with n. We shall return to the asymptotic behavior of the coefficients later when the value of $\lambda_\star$ has been determined more accurately.

At this point, we would like to emphasize that all coefficients we computed were calculated in an algebraically exact way using *Mathematica*'s symbolic manipulation capabilities. This turned out to be crucial because numerical errors would spoil the picture dramatically. Due to the recursive character of the calculation, any rounding errors accumulate. This became manifest in Figure 2(b), for instance, where a more-than-exponential growth is suggested if calculations are done numerically, and it is particularly true for the findings of the next section.

Before we double-check the solution by re-inserting it into the β function, i.e. the right-hand side of (1.24), we would like to point to an interesting property of the signs of the individual coupling constants c_n.

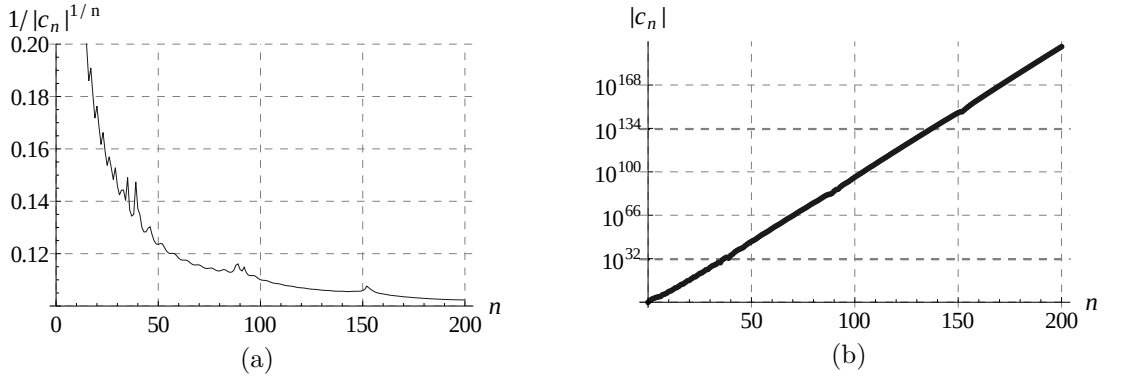

Fig. 2: Convergence behavior of the Taylor-like series for the fixed point potential; (a) the quantity $1/\sqrt[n]{|c_n|}$ as a function of the order n. This should yield the radius of convergence ρ_c in the limit $n \to \infty$; (b) logarithmic plot of the absolute value of the series' coefficients.

2.1.3 Sign Structure of the Coupling Constants

With $\lambda_\star = -0.186\,064\,200$ being the best guess for the mass parameter c_1 so far, we would like to investigate the alternating behavior of the coefficients c_n of the series expansion. The solutions to many problems in physics are described by alternating (asymptotic) series [32,33]. Since we are unable to solve the recurrence relation (2.6), we may try to find an analytic expression that approximates the coefficients c_n in the limit $n \to \infty$. In the previous section, we conjectured that the absolute values of the coefficients grow exponentially. To complete the picture, it seems natural to investigate the sign structure of these coefficients, too. Furthermore, it will allow us to confirm and fine-tune the value of $\lambda_\star$.

At a first glance, the sign structure of the c_n seems to be rather random. However, due to the approximative character of our choice of $\lambda_\star$, we shall probe this structure for small deviations of λ from its previously fixed value. Consider Figure 3(a), for example, where we plotted the sign of the nth coefficient as a function of λ as a dark $(+1)$ or light (-1) pixel in a rectangular grid. Here, we vary λ in the sixth digit, and the coefficients of orders 50 through 100 are displayed. It can be seen that the value of $\lambda_\star$ (i.e. $\Delta\lambda = 0$) indeed marks a change of sign for many coefficients. Nevertheless, this is in fact not surprising because we chose $\lambda_\star$ to be an (approximate) root of the c_n, so that a change of sign is rather likely.

Therefore, consider now Figure 3(b) where we have zoomed in on the critical region, varying λ in the eigth digit of $\lambda_\star$ for each pixel. It turns out that our view on the sign structure was too vague. At this stage, we find that the border zone is more complex than it looked like in the first place. Furthermore,

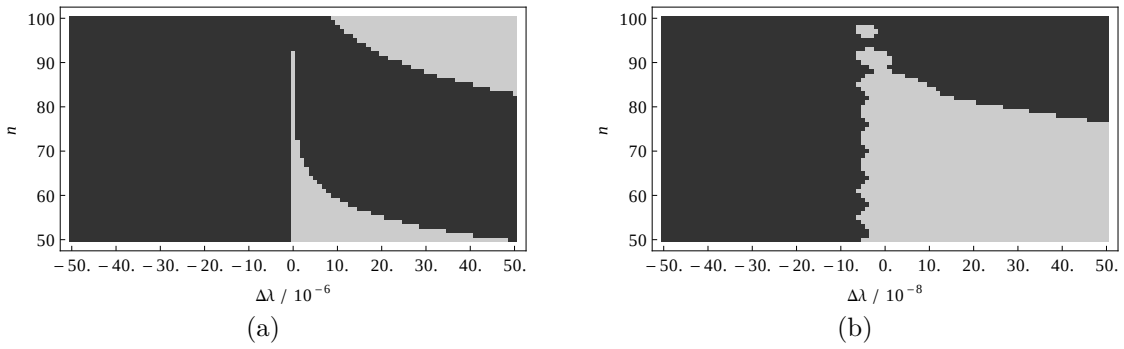

Fig. 3: Visualization of the sign structure of the coefficients c_{50} through c_{100} of the small field series for different values of the parameter λ. Light: -1; dark: $+1$. On the horizontal axis, the deviation $\Delta\lambda = \lambda - \lambda_\star$ from $\lambda_\star = -0.186\,064\,20$ is recorded. For each pixel, $\lambda_\star$ is varied in the (a) sixth digit and (b) eigth digit, respectively.

we are tempted to correct our estimate of $\lambda_\star$: Guided by the idea of an alternating pattern, the actual border appears to lie about $5{\times}10^{-8}$ units to the left from the original value. This observation is supported by an even closer look at the critical region—we refer to Appendix A for a more complete and detailed picture of the sign structure of the first 200 coefficients. Setting $\lambda_\star = -0.186\,064\,250$ from now on, we find an (almost) regular structure where sign changes occur in every third term. In addition, we can limit the uncertainty of this value to ± 2 in the last digit in order to maintain this pattern.

This sign change in every third coefficient is almost perfect. Nevertheless, calculating the first 1000 coefficients for fixed $\lambda = \lambda_\star$, we find an additional '+' every 127th term, the first occurence of four positive terms in a row being c_{123} through c_{126}. Moreover, the first three terms, c_0, c_1, and c_2, are out of line, too. Hence, apart from these first three coefficients, the sign structure is periodic in 127 with each period being sub-periodic in 3 except for the last four terms all being positive. This pattern is confirmed up to order $n = 1000$.

A further investigation, however, shows that this notion is not exact either. There is a change to extra '$-$' terms at $n = 1139$ and back to '+' irregularities at $n = 1898$, but this variation could also be caused by a deviation of $\lambda_\star$ from the actual fixed point value. Anyhow, we can only speak of an approximate 127-periodic structure with a 3-periodic substructure. We shall come back to this intriguing (ir)regularity in the next sections because it turns up in other contexts, too.

2.1.4 Deviation from the Fixed Point and Radius of Comvergence

In order to check the quality of the approximation, we plug the truncated series back into the right-hand side of (1.24) and thus calculate the global β function. The result is plotted in Figure 4 for several different truncations. We understand that the convergence of the series seems to improve as the truncation n_{trunc} is increased. However, all of the approximations drift away from the fixed point at $\rho \lesssim 0.1$.

To quantify these observations, we define the maximum absolute deviation δ and the total deviation Δ of the β function in an interval (a, b):

$$\delta_{(a,b)}v := \max_{\rho\in(a,b)} \left|\beta(v)|_\rho\right| \; ; \qquad \Delta_{(a,b)}v := \int_a^b \mathrm{d}\rho \left|\beta(v)|_\rho\right| \; . \tag{2.8}$$

These quantities will be used to compare different approximation schemes later, too. Evaluating in the interval $(0, 0.1)$, we find good convergence up to an order of truncation of about 130, as can be seen in Figure 5(a). For all $n_{\text{trunc}} = 20 \ldots 130$, we obtain $\Delta_{(0,0.1)} < 2 \times 10^{-5}$. For certain choices of n_{trunc}, namely $n_{\text{trunc}} = 55, 57, 62$, the total deviation is reduced to $\Delta_{(0,0.1)} < 1 \times 10^{-7}$. For $n_{\text{trunc}} > 130$, the deviations increase, and so does the oscillatory behavior. However, the integration was performed numerically, so that the strong oscillations in particular were presumably caused by numerical errors.

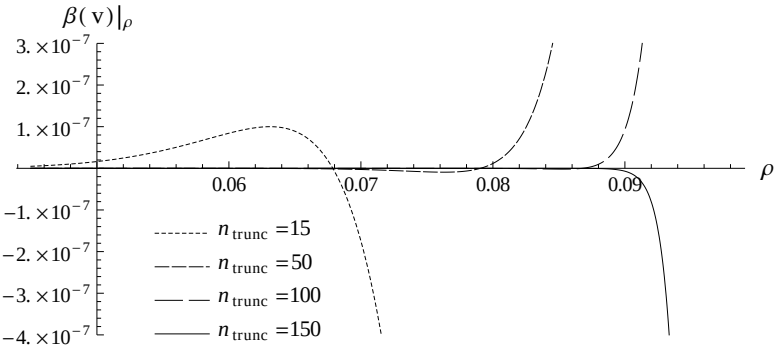

Fig. 4: Flow of the effective potential for different truncations of the asymptotic series; $\beta(v) = 0$ is desired for a fixed point.

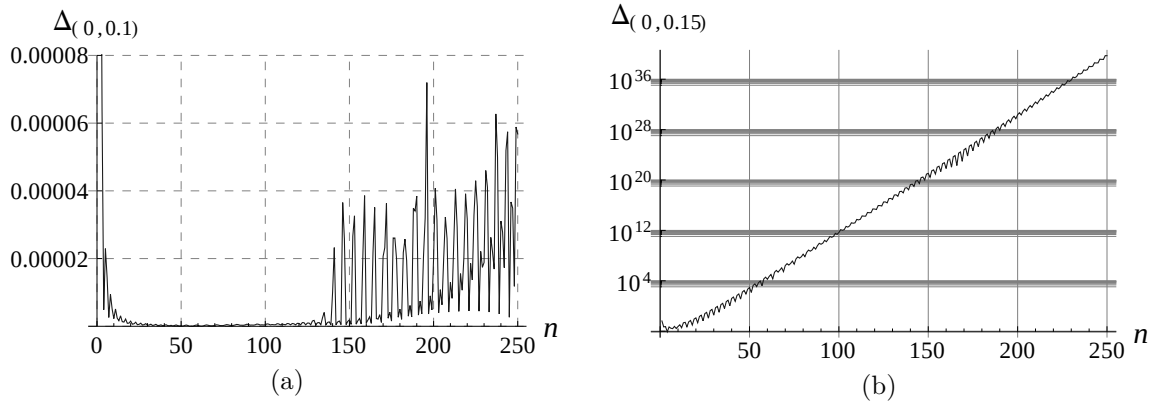

Fig. 5: The total deviation from the fixed point as a function of the order of truncation $n = n_{\text{trunc}}$. In (a), the considered interval is $(0, 0.1)$, and convergence is good up to $n \approx 130$ when numerical errors become predominant. In (b), the interval is extended to $(0, 0.15)$, and the deviation grows exponentially with the order of truncation.

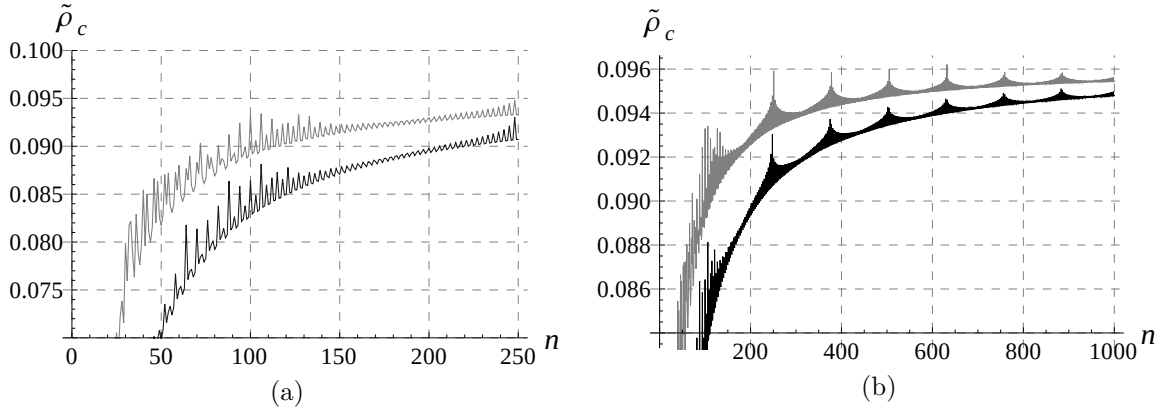

Fig. 6: The empirical radius of convergence $\tilde{\rho}_c$ as a function of the truncation $n = n_{\text{trunc}}$. The threshold $\delta_{\max}$ is 10^{-11} for the black curve and 10^{-8} for the gray curve. In (a), a close-up of the region $n = 50 \ldots 250$ is shown; in (b), ρ_c is plotted up to $n = 1000$.

In Figure 5(b) we extended the interval to $(0, 0.15)$. Note that the Δ-axis is now scaled logarithmically. Apparently, the approximation does not hold very far beyond $\rho \simeq 0.1$, and lower-order truncations, if any, should be chosen to approximate the potential in this region. More precisely, we expect to find a singularity in the complex ρ-plane at a distance $\rho_c \approx 0.1$ from the origin.

To verify this notion, we define an empirical radius of convergence

$$\tilde{\rho}_c := \sup \left\{ \rho \in (0, \infty) : \delta_{(0,\rho)} < \delta_{\max} \right\} \tag{2.9}$$

for some threshold value $\delta_{\max}$. In other words, $\tilde{\rho}_c$ is the maximum ρ for which the absolute deviation from the fixed point stays below the threshold value $\delta_{\max}$. Hence, we define another criterion of convergence based on the maximum (local) deviation δ rather than the total deviation Δ.

The result obtained from evaluating this for various truncations is affirmative. As shown in Figure 6(a), the empirical radius of convergence is an overall increasing function of the truncation, and this observation is independent of the choice of the threshold value $\delta_{\max}$. Taking into account the above calculated total deviations, we are tempted to choose the optimum truncation $n_\star$ such that $n_\star < 130$. In this case, we get $n_\star = 106$ with $\tilde{\rho}_c = 0.088$ for $\delta_{\max} = 10^{-11}$ or $n_\star = 94$ with $\tilde{\rho}_c = 0.091$ for $\delta_{\max} = 10^{-8}$, respectively. However, the values of $\tilde{\rho}_c$ are all close to each other in the range $n_{\text{trunc}} = 80 \ldots 130$ as are the total deviations, and thus the concept of an optimum truncation is rather meaningless in this case.

An extended view of $\tilde{\rho}_c$ in Figure 6(b) suggests an actual radius of convergence of about 0.095. Furthermore, this figure reveals the pattern of periodicity we detected in the previous section again. As did the signs of the coefficients, the empirical radius of convergence oscillates with one peak followed by two dips, showing an approximative 3-periodic structure. Moreover, this structure itself exhibits peak values every 127 terms.

Having a vague idea of the sign structure of the c_n and its influence on the series, we also want to analyze the asymptotic behavior of the coefficients' absolute values. We already noted in Figure 2(b) that the c_n appear to grow exponentially with n. This impression is retained for the slightly modified value of the parameter $\lambda_\star$, and hence we shall try a linear fit of the form

$$\ln|c_n| \sim \alpha_0 + \alpha_1 n\,. \tag{2.10}$$

Considering the first 1000 coefficients, this yields $\alpha_0 = -16.46(8)$ and $\alpha_1 = 2.33741(10)$. According to (2.7), the radius of convergence is

$$\rho_c = 1/\lim_{n\to\infty} \sqrt[n]{|c_n|} \sim 1/\lim_{n\to\infty} \sqrt[n]{\mathrm{e}^{\alpha_0+\alpha_1 n}} = \mathrm{e}^{-\alpha_1}\,, \tag{2.11}$$

which evaluates to $\rho_c = 0.096\,577(10)$ in the given case. In the next section, we shall substantiate this assumption by means of an analysis of the functions complex singularities.

2.1.5 Resummation and Special Points

Power series like the small field expansion calculated here have very limited convergence properties. A general result of complex analysis is that for any function which has singularities in the complex plane, its power series representation is convergent in a circle around the expansion point whose radius is determined by the distance to the nearest singularity from this point [34, p. 204]. However, even divergent series still carry information about the function they represent, and the aim of resummation techniques is to make this information available beyond the (potentially vanishing) radius of convergence, and to accelerate convergence in general [33, 35].

The method of *Padé approximants* is particulary useful to extend the region of convergence or to obtain other information such as the location of singularities and branch points of the function considered [35–39]. An application of the technique to various nonlinear ODEs can be found in [15], where the analysis of special points is put into action, too.

The idea of Padé approximation is rather simple seeing as the obvious lack of a power series is its inability to account for the function's singularities. Instead of a polynomial, we thus try to use a rational function to approximate the potential v around the origin:

$$\mathcal{P}_{[M/N]}v(\rho) = \frac{a_0 + a_1\rho + \ldots + a_M\rho^M}{1 + b_1\rho + \ldots ... + b_N\rho^N} \tag{2.12}$$

The parameters a_i and b_j are to be chosen in such a way that the first $M + N + 1$ coefficients of a Taylor expansion of (2.12) match with those of the original function v, i.e. [39]

$$v(\rho) - \mathcal{P}_{[M/N]}v(\rho) = \mathcal{O}\left(\rho^{M+N+1}\right) \quad \text{as} \quad \rho \to 0\,. \tag{2.13}$$

Therefore, we can calculate the $[M/N]$ Padé approximant of v from the coefficients $c_0, \ldots, c_{n_{\mathrm{trunc}}}$ of the small field expansion where $n_{\mathrm{trunc}} = M + N$. A detailed description of this procedure is given in Appendix B. All approximants may be collected in the so-called *Padé table* with the $[M/N]$ approximant in the Mth row and Nth column.

Three examples of Padé approximants to the truncated series with $n_{\mathrm{trunc}} = 15$ are plotted in Figure 7(a), and Figure 7(b) shows their deviation from the fixed point. Here we observe that the Padé expressions do not improve convergence significantly although the deviation from the fixed point is reduced slightly. The majority of the entries in the Padé table exhibits poles on the positive real line, especially when going to higher orders.

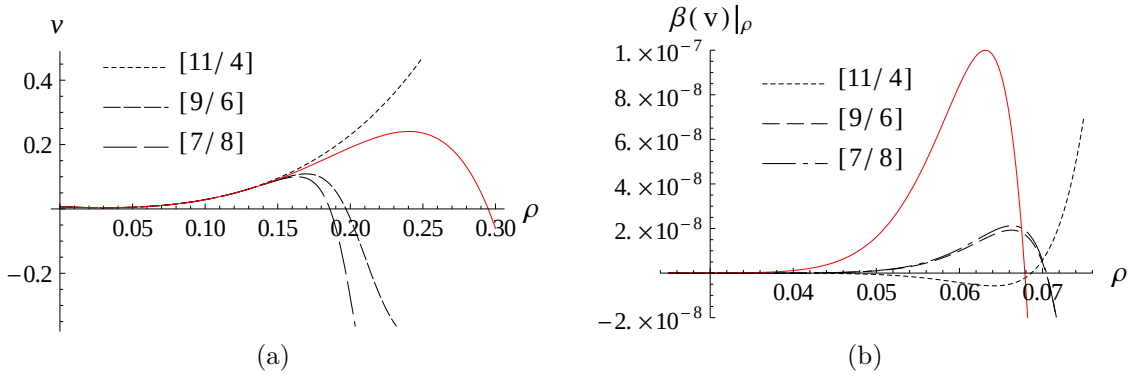

Fig. 7: (a) Padé approximants of order $M + N = 15$ to the small field expansion of the fixed point potential and (b) their deviation from the fixed point. For comparison, the corresponding small field series graphs with $n_{\text{trunc}} = 15$ are plotted in red in both panels.

We would like to mention at this point that there exists a powerful procedure related to Padé approximation that provides a way to determine unknown parameters such as the mass coefficient λ in our case. We understand that a series expansion and its Padé approximant agree up to the $(M+N+1)$-th coefficient of the series. The idea of the *Padé-Hankel method* is to estimate the free parameter by enforcing this matching condition on the next order as well [15, 40]. We shall not dwell on this method here because it does not change the general picture. Instead, we refer to Appendix B.3 for now, but we shall come back to this concept in Section 3.4, too. Here we only note that we find $\lambda_\star = -0.186\,064\,249\,4\ldots$ by this procedure using the first 45 terms of the series, which is a dramatic increase in accuracy compared to solving for roots of the c_n directly as done in Section 2.1.2.

Let us rather discuss the distribution of poles and zeros of the Padé expressions for it reveals many additional properties of the function they approximate, too. In particular, the structure of singularities and branch points is approximated [36, pp. 44-56]. So despite the fact that we are unable to extend the solution significantly by the method of Padé, we can still extract useful information from the approximants.

We note that it might happen that roots of the numerator and the denominator of an approximant coincide, effectively reducing the degree of either one. These are called *ghost pairs* [38] or *defects* [36, 37]. Furthermore, the respective leading order coefficients $a_M, a_{M-1}, \ldots$ and $b_N, b_{N-1}, \ldots$ may vanish as a result of solving the corresponding system of equations. Thus the exact degrees of the numerator and denominator may be different from those assumed by the ansatz (2.12). The *defect* of the $[M/N]$ approximant is defined by

$$d_{[M/N]} := \min\{M - M', N - N'\} \tag{2.14}$$

where M' and N' denote the exact degrees of the numerator and denominator of the Padé approximant. The operator $\mathcal{P}_{[M/N]}$ is continuous at v with respect to the supremum norm if and only if $d_{[M/N]} = 0$ [41, p. 109]. Although we do not exactly know v or, more precisely, its Taylor coefficients c_n, continuity of the Padé operator assures that for small deviations of the c_n, the deviation of the corresponding a_i and b_j from the "exact" values remains small as well.

Unfortunately, we will see that in the case considered here, the approximations exhibit lots of potential defects where zeros and poles virtually coincide. They are usually caused by an almost singular system of equations to determine the Padé coefficients [37]. This should be kept in mind in the following discussion. Most of the Padé table was calculated numerically, but the results were checked qualitatively against exact computations for certain approximants up to order $M + N = 43$.

Coming back to the Padé approximants of the fixed point series expansion, a typical distribution of poles and zeros is displayed in Figure 8. Here we plotted the $[N+3/N]$ approximants in anticipation of the large-order behavior of the fixed point potential, $v(\rho) \sim \rho^3$ as $\rho \to \infty$ (cf. Section 2.2). However,

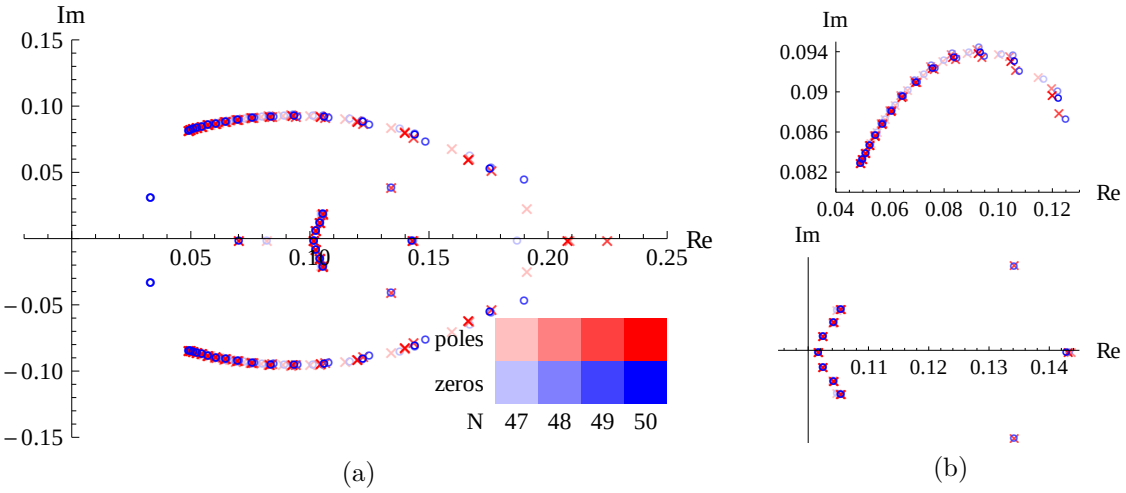

Fig. 8: Distribution of poles and zeros of the $[N+3/N]$ Padé approximants for $N = 47, \ldots, 50$; (a) the full interesting region; (b) close-up of the top wing and the central cut.

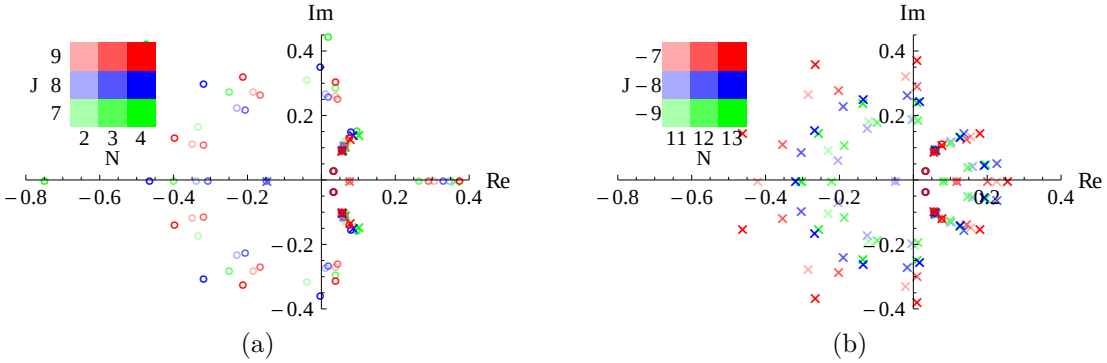

Fig. 9: Distribution of poles and zeros of the $[N + J/N]$ approximants in the off-diagonal region of the Padé table. Poles are marked by "×", zeros by "∘"; (a) $J > 0$, such that there are more zeros than poles; (b) $J < 0$, extra poles.

there is no evidence from the small field Padé table that this particular choice of $M - N = 3$ is singled out. The picture of any close-to-diagonal approximant is essentially the same.

Of course, the distribution of poles and zeros is symmetric with respect to the real line because the coefficients a_i and b_j are real. From the left panel, we notice two distinctive structures. On the one hand, there are two wings of poles and zeros accumulating at $\rho \approx 0.05 \pm 0.08\,\mathrm{i}$. On the other hand, we find a second cut in the center at $\rho \approx 0.10$. A close-up of the two regions is plotted in the right panel. Besides these two salient regions, a number of potential ghost pairs that show no converging behavior arise. Refering to the above remark, this casts doubt on the continuity of the Padé operator.

Of the two prevailing clusters of poles and zeros, the wings are already manifest in the diagonal $[N/N]$ sequence at $N \approx 5$. The central cut however only shows up at $N \approx 20$. This suggests that the wings are the dominant structure of the potential v whereas the central cut may either be a spurious feature of the approximation or be suppressed at lower orders.

This notion is further emphasized if we consider the situation away from the diagonal of the Padé table, plotted in Figure 9. In this case, an equal number of poles and zeros accumulate in the wing region again. Extra zeros, however, arrange in a semicircle in the left part of the complex plane. The same is true for additional poles, but some of the poles cluster at the edges of the central cut, too.

The fact that the wings are marked by a sequence of poles and zeros that tend to merge in one point at $\rho_\pm = 0.049 \pm 0.083\,\mathrm{i}$ suggests that the original function v has branch points at $\rho = \rho_\pm$ [36, p. 47]. The

line of poles and zeros then models the corresponding branch cut such that the region of convergence is maximized in some sense [42]. This conception is supported by the considerations of Appendix B.2, as well. The distance of these branch points from the origin determines the radius of convergence of the small field series expansion. For $M + N \simeq 100$ we find $|\rho_\pm| \approx 0.096455$, which is in agreement with the results of the previous section.

Moreover, we believe that the location of the branch points can be related to the sign structure of the coefficients c_n of the small field series: Consider a function f of the form

$$f(\rho) = \frac{1}{2}\left(1 - \alpha\, \mathrm{e}^{\mathrm{i}\Omega}\rho\right)^\gamma + c.c. \tag{2.15}$$

with $\alpha > 0$, Ω and γ real. We added the complex conjugate in order that the function is real for real values of ρ. For $\gamma \notin \mathbb{Z}$, this function has branch points at $\rho = \mathrm{e}^{\pm\mathrm{i}\Omega}/\alpha$. Expanding at $\rho = 0$, we get

$$f(\rho) = \frac{1}{2}\sum_{n=0}^{\infty} \frac{(-1)^n}{n!}\left[\prod_{i=0}^{n-1}(\gamma - i)\right] \alpha^n \mathrm{e}^{\mathrm{i}\Omega n}\rho^n \; + \; c.c.\,,$$

which may be written

$$f(\rho) = \sum_{n=0}^{\infty} \frac{(-1)^n}{n!}\left[\prod_{i=0}^{n-1}(\gamma - i)\right] \alpha^n \cos(\Omega n)\rho^n\,. \tag{2.16}$$

As soon as $n > \gamma$, the terms in square brackets alternate in sign with n. Since $\alpha > 0$, these oscillations are canceled by the factor $(-1)^n$, and the only term affecting the sign structure of the series coefficients is $\cos(\Omega n)$; if $\Omega = \pi/\kappa$, the sign of the coefficients changes every κ terms.

In Section 2.1.3 we found that the signs of the c_n change approximately every three terms, thus suggesting $\kappa \approx 3$ for the series of v. From the close-to-diagonal Padé approximants of order $M + N = 100$ we determined the argument of the branch points' locations to be $\Omega \approx 1.037$. This corresponds to a value of $\kappa \approx 3.031$. Hence, the sign structure is approximately, but not exactly 3-periodic. We can write it as $\Omega = \frac{\pi}{3}\left(1 - \frac{1}{K}\right)$ with $K = 98.53$, which leads to a 3-periodic structure that is delayed in such a way that approximately every 98 or 99 terms an additional fourth term of the same sign occurs. This is not quite $K \approx 127$ which we would expect from the actual behavior observed above, but it is reasonably close.

We also recall that c_0, c_1, and c_2 did not follow the pattern of the rest of the coefficients. We found from (2.16) that the structure of the c_n is solely determined by Ω for $n > \gamma$. Thus we may assume $\gamma < 3$ locally around the origin. However, the average potential v is obviously not of the simple form (2.15), and other effects influence the sign structure of the coefficients. Most strikingly, this approach does not reflect the large-order behavior to be examined in Section 2.2.

2.1.6 The Vacuum Expectation Value

To finish up with the small field limit, we would like to collect some properties of the potential that can already be read off this approximation. The vacuum energy $v(0)$ given by the coefficient c_0 is determined as $0.006\,915\,7\ldots$; of course, this does not contain any physical information, we merely note it down in order to compare it to later results.

More interesting from a physical point of view is the vacuum expectation value ρ_0 corresponding to the minimum of the potential because the behavior of the potential in the vicinity of ρ_0 determines the macroscopic properties of the system. In a more sophisticated next step, one could try to restore space-time dependence of the field ρ by considering fluctuations around the vacuum expectation value, $\rho(x) = \rho_0 + \delta\rho(x)$, leading to corrections to the effective action.

The location of the minimum lies well inside the region of convergence. We find $\rho_0 = 0.0306\ldots$ for all expansions with $n_{\mathrm{trunc}} \geq 5$, and $\rho_0 = 0.030\,647\,9(5)$ for $n_{\mathrm{trunc}} \geq 10$. This reinforces the notion that

the expansion is a reliable approximation up to a certain distance from the origin. The associated value of v is $v_{\min} = v(\rho_0) \approx 0.003\,860\,87(1)$.

2.2 Large Field Asymptotics

The approximate expressions obtained in the last section all break down at $\rho \lesssim 0.1$. As another limiting case, we would like to discuss (2.1),

$$3v - \rho v' = \frac{1}{6\pi^2} \frac{1}{1 + v' + 2\rho v''}\,, \tag{2.1'}$$

in the large-field limit $\rho \to \infty$.

2.2.1 Series Expansion

Assuming $\rho \gg 1$, we investigate the leading order behavior using the method of dominant balance first. To lowest order, neglect the right-hand side, i.e.

$$\frac{1}{1 + v' + 2\rho v''} \ll 3v, \rho v' \qquad (\rho \to \infty)\,. \tag{2.17}$$

Consequently, setting the left-hand side equal to zero, we find

$$v_{(0)}(\rho) = A\rho^3\,, \tag{2.18}$$

where A is a real constant to be fixed later. It must be positive in order to ensure that the potential is asymptotically convex. Apparently, this result for the leading order is consistent with the assumption (2.17). We see that the large-field behavior is dominated by the scaling part of the flow equation. To proceed, we could follow the route of [43] and continue with a perturbative expansion, thus plugging $v = v_{(0)} + v_{(1)}$ into the left-hand side of (2.1) and substitute $v = v_{(0)}$ on the right-hand side to calculate $v_{(1)}$, and so on. However, for computational reasons, it turns out to be advantageous to start with a power series expansion

$$v(\rho) = \sum_{n=n_0}^{\infty} C_n \rho^{-n} \tag{2.19}$$

and derive a recurrance relation for the coefficients C_n again. Note that we do not start the series at $n = 0$ but rather at some arbitrary n_0. To be consistent with (2.18), we expect to find $n_0 = -3$.

Inserting the series expansion into (2.1) and sorting by powers of ρ, we get

$$\begin{aligned} &\sum_{r=2n_0+1}^{n_0-1} \rho^{-r} \sum_{n=n_0}^{r-n_0-1} (r-n+2)(2n+1) n C_{r-n-1} C_n \\ &\quad + \sum_{r=n_0}^{\infty} \rho^{-r} \left[(r+3) C_r + \sum_{n=n_0}^{r-n_0-1} (r-n-2)(2n+1) n C_{r-n-1} C_n \right] \stackrel{!}{=} \frac{1}{6\pi^2}\,. \end{aligned} \tag{2.20}$$

The first term on the left-hand side occurs if and only if $n_0 \leq -1$. Comparing to the right-hand side, the inner sum over n must then vanish for all r. The smallest possible n_0 is thus found by setting $r = 2n_0 + 1$ whence the inner sum contains only one term,

$$\rho^{-(2n_0+1)} (n_0 + 3)(2n_0 + 1) n_0 \, C_{n_0}^2 \stackrel{!}{=} 0\,.$$

The only integer solution consistent with the precondition $n_0 \leq -1$ is then $n_0 = -3$. Hence we have recovered the previously found leading order behavior. Choosing $C_{-3} := A$ as our free parameter, we

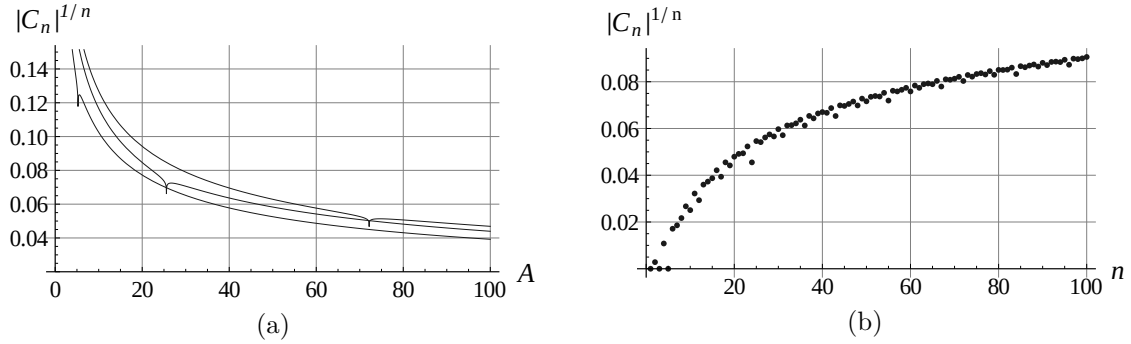

Fig. 10: Converging behavior of the large field series; (a) n-th root of the n-th coefficient as a function of the parameter A. This quantity converges to R_c as $n \to \infty$. From top to bottom, we have $n = 70$, $n = 55$, $n = 40$; (b) n-th root of the n-th coefficient as a function of the order n for the optimum parameter $A_\star = 28.067$.

can successively calculate all other C_n. The next non-vanishing coefficient is C_2 obtained from the ρ^0 term,

$$C_2 = \frac{1}{450\pi^2 A}\,. \tag{2.21}$$

All other coefficients can be calculated recursively again: For $r = 1, 2, \ldots$,

$$C_{r+2} = \frac{-1}{15(r+5)A}\left[(r+3)C_r + \sum_{n=-2}^{r+1}(r-n+2)(2n+1)nC_{r-n-1}C_n\right]\,. \tag{2.22}$$

The resulting series is

$$v(\rho) = A\rho^3 + \frac{1}{450\pi^2 A\rho^2} - \frac{1}{9450\pi^2 A^2\rho^4} + \frac{1}{182\,250\pi^2 A^3\rho^6} - \frac{1}{607\,500\pi^4 A^3\rho^7} + \ldots\,, \tag{2.23}$$

the same result as obtained form a perturbative expansion and in accordance with [43] taking into account the different units (see also Appendix C).

2.2.2 Radius of Convergence

As in the weak-field case, we are left with one free parameter, the leading order coefficient A. It would be nice to find a similar procedure as before, i.e. a way to determine the value of A such that the convergence of the series (2.23) is optimum. From [34, p. 213] together with (2.7), an inverse power series

$$v(\rho) = A\rho^3 + \sum_{n=1}^{\infty} C_n\rho^{-n} \tag{2.24}$$

like (2.23) converges for all $\rho > R_c$ with

$$R_c = \limsup_{n\to\infty} \sqrt[n]{|C_n|}\,. \tag{2.25}$$

Unfortunately, the roots of the C_n do not exhibit a converging structure with increasing order unlike it was in the small field case. Moreover, R_c shows an overall decrease with increasing A because the singularities at $\rho = 0$ from negative powers are suppressed (see Figure 10(a)).

However, the coefficients C_n decrease rapidly with increasing n such that there is hope to find a relatively large region of convergence. Indeed, Figure 10(b) suggests that it extends extends to $\rho \simeq 0.1$.

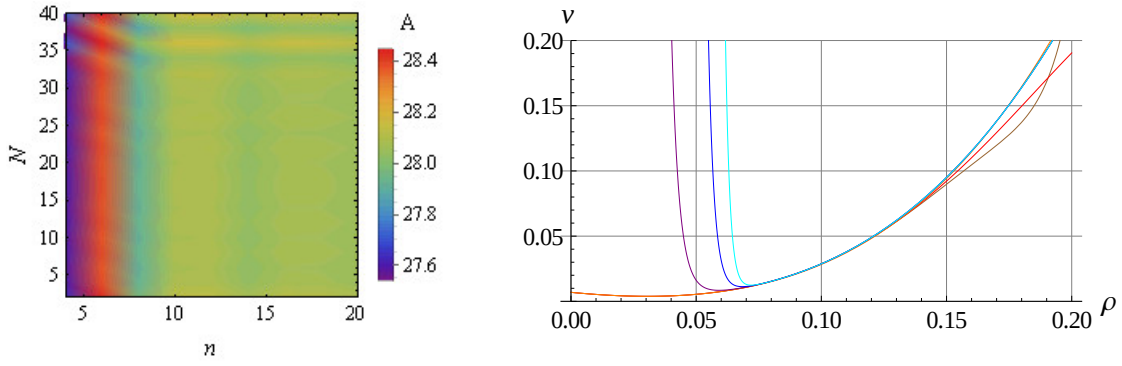

(a) (b)

Fig. 11: (a) Value of the parameter A such that Δ_{SL} is minimized in the connecting interval $(0.08, 0.10)$ for different orders n of the small field and N of the large field series expansions; (b) small and large field series expansions around the connecting interval $(0.08, 0.10)$, where A was determined such that Δ_{SL} is minimum. Small field truncations: $n = 4$ (orange), $n = 7$ (red), $n = 15$ (brown); large field truncations: $N = 10$ (purple), $N = 20$ (blue), $N = 30$ (cyan).

In the plot, A was chosen as the optimum parameter that we shall determine in the next section, but it should be seen as an example here; the qualitative picture is essentially the same independent of A.

Given that the radius of convergence reaches to a region where we found the small field series to yield confidable results, we shall determine the constant $A_\star$ that describes the potential at the Wilson-Fisher fixed point by minimizing the difference between the small and large field series in a connecting interval (ρ_1, ρ_2). That is to say, we minimize

$$\Delta_{SL}^2(A) = \int_{\rho_1}^{\rho_2} \mathrm{d}\rho \, [v_{S,n}(\rho) - v_{L,N}(\rho)]^2 \tag{2.26}$$

in a region where both expansions can be considered reliable. Here $v_{S,n}$ denotes the small field asymptotic series up to order $n_{\text{trunc}} = n$, and $v_{L,N} = v_{(0)} + \ldots + v_{(N)}$ is the large field approximation of order N in the perturbation series, i.e. $v_{(k)}$ is the kth non-vanishing term in the series (2.24). The connecting interval should be chosen in such a way that both approximations can be assumed reliable; we use $(\rho_1, \rho_2) = (0.08, 0.10)$ for now and check this assumption later.

In Figure 11(a) we display the optimized value of A depending on different truncations of the small and large field series expansions. It can be seen that it stabilizes around $A = 28.0 \ldots 28.1$ as n and N are increased. The fluctuations for values $N > 30$ are due to the singularity of the approximation $v_{L,N}$ at $\rho = 0$. Note that the actual radius of convergence of the inverse power series lies outside the connecting interval, such that the influence of the singularity increases with N.

Averaging in the region $n = 10 \ldots 20$, $N = 5 \ldots 30$, we find $A_\star = 28.067(25)$; this will become our choice for the parameter A from now on. It agrees with the results $A_\star = 28.05$ from [44] and $A_\star = 28.054$ in [43] after a conversion of units (Appendix C).

In order to justify the choice of the connecting interval, take a look at Figure 11(b) where we plotted the series expansions $v_{S,n}$ and $v_{L,N}$ for various truncations n and N. Obviously, the small and large field approximations coincide in the interval $\rho = 0.08 \ldots 0.13$. Note, however, that this consistency interval shrinks as either n or N are increased. Shifting the connecting interval (ρ_1, ρ_2) to the right within this range does not affect the value of $A_\star$ within the confidence interval given above.

2.2.3 Deviation from the Fixed Point

Next, we would like to check how well this large field approximation satisfies the fixed point condition $\beta(v) = 0$. Using the leading order term $v_{(0)}(\rho) = A\rho^3$ only, the expression is analytic on the whole

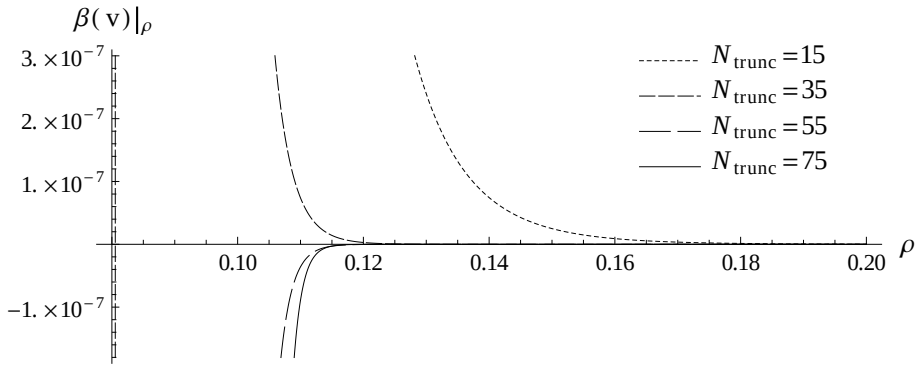

Fig. 12: Flow of the effective potential for different truncations of the large field perturbation series; $\beta(v) = 0$ is desired for a fixed point.

real line. The flow β can be computed straightforwardly in this case, and we find

$$\beta(v_{(0)}) = \frac{1}{6\pi^2}\frac{1}{1+15A\rho^2}\,. \tag{2.27}$$

For this expression, we can calculate the total deviation $\Delta_{(0,\infty)}v_{(0)}$ as defined in (2.8), which can be considered to provide an upper bound for a meaningful global approximation to be found. Here

$$\Delta_{(0,\infty)}v_{(0)} = \int_0^\infty \mathrm{d}\rho\,\big|\beta(v_{(0)})|_\rho\big| = \frac{1}{12\pi\sqrt{15A}}\,, \tag{2.28}$$

which evaluates to approximately 0.0013 for $A = A_\star = 28.067$. Apparently, the larger we choose A, the better our solution conforms with the fixed point equation. This provides another explanation of the difficulties to determine $A_\star$ from the series' intrinsic properties.

If more terms of the series (2.24) are included, the deviation becomes infinite due to the singularity at the origin, of course. Nevertheless, we can still analyze the converging behavior by reinserting the truncated series into (2.1). The resulting flow $\beta(v)$ is plotted in Figure 12 for various truncations N_{trunc}. We see that the maximum deviation in the interval $(0.15,\infty)$, $\delta_{(0.15,\infty)}v$, remains smaller than 3×10^{-8} for $N_{\mathrm{trunc}} \geq 15$. This is a remarkable result seeing as the solution was obtained in the limit $\rho \gg 1$.

Furthermore, we can calculate the total deviations $\Delta_{(0.1,\infty)}v$ for different truncations, extending the lower bound of the interval to 0.1. We find that $\Delta_{(0.1,\infty)} < 3\times10^{-7}$ for $N_{\mathrm{trunc}} \geq 10$. This should be compared to $\Delta_{(0,0.1)} < 1\times10^{-7}$ obtained from the optimum truncations of the small field series on the remaining part of the positive real axis, $(0, 0.1)$. Combining the two approximations, we can thus specify the fixed point potential up to a total deviation $\Delta_{(0,\infty)} < 4\times10^{-7}$.

All in all, these findings further justify our rather bumbling method to obtain the optimum value of $A = A_\star$. Indeed, we shall be able to recover some properties of the small field series in the next section.

2.2.4 Improvement of Convergence

If we extend our discussion of the total deviation from the fixed point to the interval $(0.01,\infty)$, the limited radius of convergence of the large field solution becomes manifest again. To allow for comparison of results from this and the previous section, we note that for $N_{\mathrm{trunc}} = 20$ we get $\Delta_{(0.01,\infty)} \approx 10^{10}$, which increases further with N_{trunc}, e.g. for $N_{\mathrm{trunc}} = 40$ we find $\Delta_{(0.01,\infty)} \approx 10^{30}$.

Given that the large field series (2.23) is quite well-behaved, we shall try to extend convergence to the whole positive real axis by the method of Padé approximants again. In particular, it would be interesting to see if the large field series carries information about the potential minimum. We hope

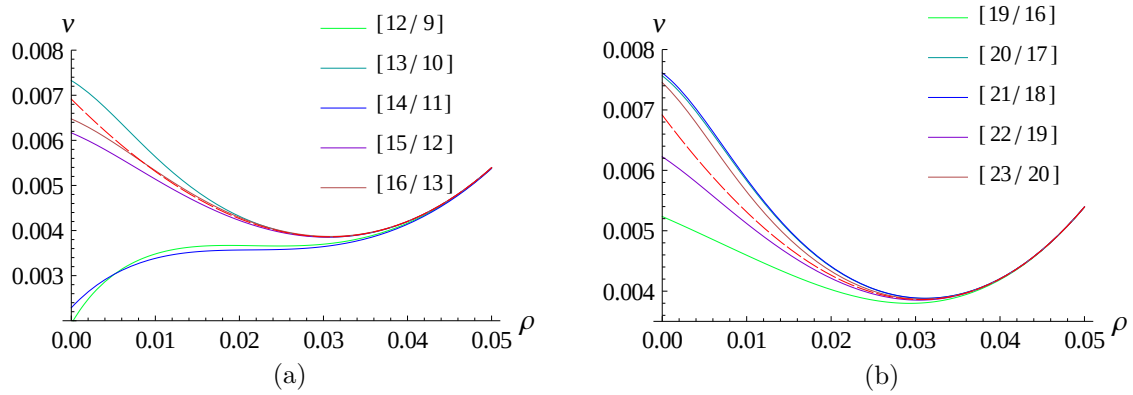

Fig. 13: Padé approximants to the large field series expansion. The $n_{\text{trunc}} = 25$ approximation of the weak field expansion is plotted in red color for comparison. Exact calculation of the coefficients was processed in (a) whereas in (b) the coefficients were calculated numerically. While the shape of the potential around its minimum is resembled quite well, convergence to the value at $\rho = 0$ does not seem to improve significantly at higher orders.

to reproduce the properties found in Section 2.1.6, namely the vacuum energy $v(0) = 0.006\,915\,7$ and the minimum of the potential $v_{\min} = 0.003\,860\,87$ at $\rho_0 = 0.0306479$.

As before, the polynomial order of the numerator and denominator are denoted M and N, respectively. In order to maintain the correct behavior in the limit $\rho \to \infty$, we restrict ourselves to Padé approximants where $M - N = 3$. The coefficients a_i, b_j are calculated by expanding the Padé ansatz around $\rho = \infty$ and comparing coefficients to the C_n as defined in (2.24). For details see Appendix B.1.2. The obtained system of equations turns out to have no solution for some of the low-order approximants, but the general result is that the method leads to well-defined analytic expressions on the whole non-negative real line.

The first useful expression is the [5/2] approximant, for which $\bar{v}(0) = 0.0047$ already hits the desired value of 0.0069 closely. Furthermore, its graph also exhibits the correct form, showing a minimum at $\bar{\rho}_0 = 0.0293$, which is reasonably close to the expected value $\rho_0 = 0.0306$, too. Increasing the order of the Padés reveals an interesting structure: the $[M/N]$ approximants where N is an even number seem to converge quickly to the correct solution, merging with the small field series. Those with odd N, however, tend to bend off towards decreasing values of $\bar{v}$ as ρ approaches 0. To illustrate this, take a look at Figure 13(a).

This behavior may be explained by the fact that the roots of a polynomial with real coefficients come in pairs of complex conjugates. Hence, for a polynomial of odd degree, there remains at least one root on the real axis. Nevertheless, we see that the [16/13] approximant converges exceptionally well; compared to the other approximant's poles, its only singularity on the real line is located "far away" from the origin at $\rho = -0.183$. Generally speaking, the effect of the extra real root is vanishing as N is increased, which can be seen from Figure 13(b). Furthermore, some Padé approximants with even N such as the [9/6] expression have two poles on the real axis.

The approximants up to order $N = 13$, visualized in Figure 13(a), were calculated by solving the corresponding system of equations exactly. Due to extensively growing computation times, we switched to numerical methods for higher orders, see Figure 13(b). We found that the approximations of order $N > 13$ did not improve convergence to the exact solution (more precisely, the small field expansion in this region), be it caused by numerical instabilities or a general limitation of the Padé method.

To quantify the quality of the approximation, we calculated the total deviation from the fixed point as defined in (2.8). Seeing as these Padé functions are analytic in the whole domain of interest, we extended the interval to the positive real axis. As expected from the graph in Figure 13, the best result is obtained for the [16/13] approximant where $\Delta_{(0,\infty)} = 1.85 \times 10^{-5}$, which is two orders of magnitude smaller than the deviation of the leading order term $v_{(0)}(\rho) = A\rho^3$ alone. The major

contribution comes from the interval $(0, 0.02)$ where $\Delta_{(0,0.02)} = 1.62 \times 10^{-5}$. The maximum deviation of the β function is $\delta_{(0,\infty)} = 1.7 \times 10^{-3}$.

The [11/8], [13/10], and [15/12] approximants all have $\Delta_{(0,\infty)} \sim 10^{-5}$. Unfortunately, all our approximations with $N \geq 14$ drift away from the fixed point as $\rho \to \infty$. We assume that this is a numerical issue since we started to use numerical methods at this order.

Lastly, it should be noted that the [16/13] Padé, being the optimum approximation so far, also reproduces the potential minimum very accurately. It is found at $\bar{\rho}_0 = 0.03079$; this is a deviation of only 0.45% from the position obtained in Section 2.1.6. The value of the Padé expression at this point underestimates the potential minimum by only 0.26%. The best values in this regard are obtained from the [13/10] approximant for which ρ_0 and $v(\rho_0)$ deviate by $+0.32\%$ and -0.13%, respectively.

Apparently, the information about the large field behavior allowed us to construct a reasonably good approximation of the fixed point potential on the whole real line. However, the deviation from the fixed point is about two orders of magnitude higher than what is obtained by directly "gluing together" certain truncations of the small and large field series at $\rho = 0.1$. Before we try to refine our global approximation, we want to have a look at the singularity structure proposed by the large field Padé functions.

2.2.5 Special Points Analysis

As before we would like to examine the locations of poles and zeros of the Padé approximants in order to get an approximate picture of special points of the potential as viewed from infinity.

As it is visualized in Figure 14, we now recognize five special points, all of which lie in a range where $|\rho| = 0.10 \ldots 0.12$. The way the poles and zeros accumulate around these points suggests that they have branch point character again. Note that the approximants were computed from a series expansion at infinity, so that the cuts are modeled by a series of poles and zeros bending off towards the origin. We also see that the choice $M - N = 3$ is singled out in this case; the typical distribution of poles and zeros along these cuts is found for $M - N \geq 3$ only. Obviously, these are the only approximants capable of reflecting the correct large-order behavior (unless several coefficients vanished).

Of the five candidates for branch points, the one on the negative real axis is presumably the weakest in the sense that it emerges last when considering entries of increasing order in the Padé table. It shows up for $N \simeq 16$ whereas the remaining four arise at $N \simeq 6$ or 7.

The fact that we find at least four special points here as opposed to only two in the small field case is astounding. Although the absolute values of the positions of these points agree, it reinforces the notion that the nature of these singular points is rather complicated. A simple branch point of the form (2.15) would appear at the very same position in a large field expansion as in the small field case, a fact that is illustrated in Appendix B.2.

We also note that a variation of the free parameter A changes the absolute value of the special points positions, but leaves the overall pattern and especially the argument of their positions unaffected. The discrepancy of special point structures as suggested by the Padé approximants of small and large field approximations therefore remains unsolved. We shall come back to it in Section 2.3.2 when we have established a global approximation making use of both limiting cases.

2.3 Global Approximation

In this section we shall incorporate information from both the small and large field series expansions to obtain a single approximating expression for the effective potential on the whole positive real axis. The method of choice are rational functions once again. These will provide improved accuracy and they will allow us to record the transition between the special point structures observed above.

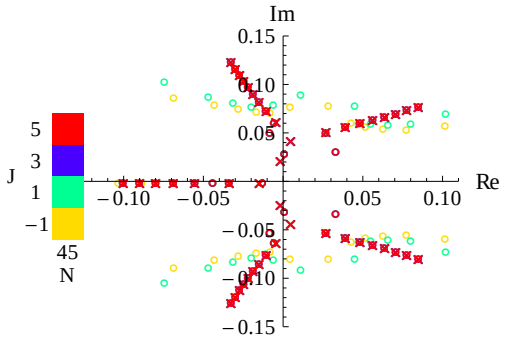

Fig. 14: Poles and zeros of the [45+J / 45] Padé approximants of the large-field series. Their distribution suggests that there are five branch points of the potential v all in a region where $|\rho|=0.10\ldots0.12$. The value $J = 3$ (markers almost completely hidden underneath the $J = 5$ ones here) stands out for marking the border between those approximants whose zeros fall into line with the poles ($J \geq 3$) and those whose zeros distribute differently ($J < 3$).

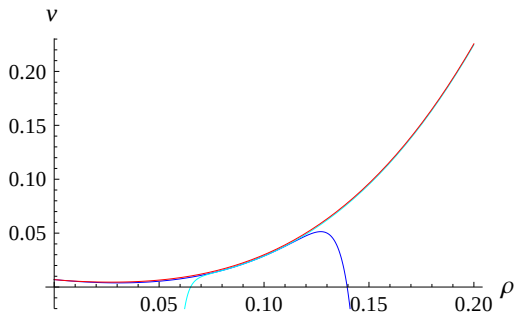

Fig. 15: Comparison of the lowest order two-point Padé approximant $[4/1]_{2,4}$ (red) to the small field (blue) and large field (cyan) truncated series with $n_{\text{trunc}} = 25$ and $N_{\text{trunc}} = 25$. In their respective domain of validity, no difference between the series expansions and the interpolating Padé function is visible to the naked eye.

2.3.1 Two-point Padé Approximation

The method of Padé approximation has yielded improvements of convergence in either of the small and large field cases. We shall go one step further and calculate a single Padé approximant that takes into account both the small and the large field series expansions. The general idea is to start from an expression like (2.12) again,

$$\mathcal{P}_{[M/N]_{r,R}} v(\rho) = \frac{a_0 + a_1\rho + \ldots + a_M\rho^M}{1 + b_1\rho + \ldots ... + b_N\rho^N} \,. \tag{2.29}$$

However, the coefficients a_i and b_j are now determined by matching the first r coefficients of a Taylor expansion of (2.29) around the origin with the small field series and the first R coefficients of a Taylor expansion of (2.29) at infinity with the large field series [35, p. 393]. Effectively, we are thus using $n_{\text{trunc}} = r - 1$ in (2.2) and $N_{\text{trunc}} = R - 1$ in (2.24), respectively. Of course, $r + R = M + N + 1$ is required for the resulting system of equations to have a unique solution. This idea is worked out in detail in Appendix B.1.3.

In the following, $[M/N]_{r,R}$ is to denote the Padé approximant of order M in the numerator and N in the denominator with truncations r and R of the contributing expansions at 0 and infinity, respectively. We shall also write it as $[M/N]_s$ where $s = \frac{R-r}{2}$ denotes the excess of included large field terms over small field terms.

Qualitatively, this method yields impressive results. Consider for example Figure 15. Here we plotted the lowest order approximant $[4/1]_{2,4} \equiv [4/1]_1$ along with the small and large field truncated series. This expression already interpolates between the two limiting cases without a noticeable deviation at the scale of the plot. Within the class of [4/1] approximants, the best result was obtained from the $s = 1$ weighting shown here. This reveals a general tendency yet to be explored in the next sections: The optimum weight (in a sense defined below) for each class has $s > 0$, but $\frac{2s}{M+N} < \frac{1}{2}$.

2.3.2 Special Points Analysis

Before we turn our attention to an investigation of the accuracy of these expressions, we would like to have a look at the poles and zeros of the two-point approximants. Seeing as their distribution was

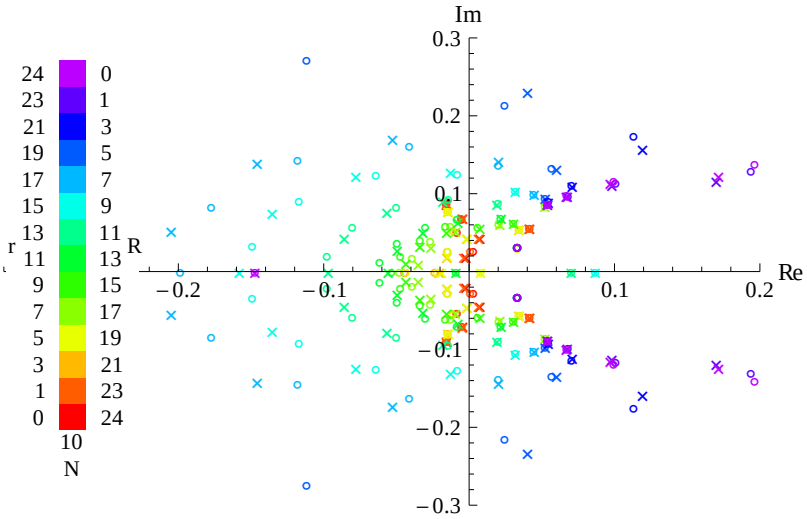

Fig. 16: Poles and zeros of the [13/10] Padé approximants for different weights of the small field series. The red markers correspond to the large-field-only weight ($R = 24$), the violet ones to the small-field-only weight ($r = 24$).

quite different in the small field and large field cases, it should be interesting to check how this picture transforms as the weight s is changed.

We monitored this transformation for the [13/10] approximants in Figure 16. A similar picture is found for other orders. Indeed, there is a smooth transition of the arrangement of special points with changing weight.

For the case of only small field terms considered, i.e. $r = 24$ or $s = -12$, we have the picture of two branch points at a distance $\rho_c \approx 0.095$ from the origin with the corresponding cuts trailing off to infinity. This was already observed in Section 2.1.5 (Figure 8). As we include more and more terms of the large field series, it seems as if these cuts combine in the negative half-plane. In other words, the cuts that were presumably connected at infinity in the small field case now lie in a finite region of the complex plane. The combination point is pushed towards the origin as s is increased.

When $r = 0$ or $s = 12$, respectively, we recover the picture of Section 2.2.5 (Figure 14). It appears from Figure 16 that the large field series' branch points in the positive half-plane correspond to the ones found for the small field series. On the contrary, the extra points in the negative half-plane that we encountered in the large field case seem to be obscured in the small field series. Alternatively, they may be interpreted as laterals of the cut itself.

2.3.3 Accuracy

In order to discuss the accuracy of these approximations, let us again consider the total deviation $\Delta_{(0,\infty)}$ on the whole positive real line as defined by (2.8) first. A graphical representation of this measure for various orders and weights is shown in Figure 17. Certain approximants exhibit poles in the interval $(0, \infty)$ and hence $\beta(v)$ diverges at these points leading to an infinite total deviation. These are marked by a dark red square. This is more likely to occur for negative or small positive values of s where the effect of the small field terms dominates.

It can be seen that the deviation generally decreases as the order is increased, thus suggesting a convergent character of the approximants. The $[4/1]_1$ term plotted above in Figure 15 has $\Delta_{(0,\infty)} = 4.3(5) \times 10^{-3}$. Notice that the integrals were evaluated numerically here. The error was approximated by varying the integration procedure and estimating the contributions from outside the integration interval, which was chosen to be $(0, 10)$.

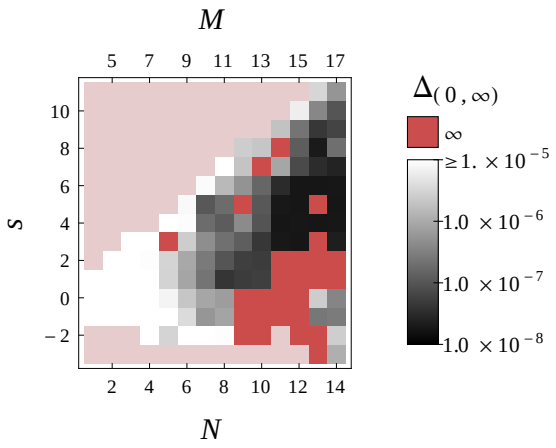

Fig. 17: Total deviation $\Delta_{(0,\infty)}$ of the $[N+3/N]$ two-point Padé approximants for different weights $s = \frac{R-r}{2}$ of the small and large field series. Expressions marked dark red have infinite deviation due to poles on the positive real axis. Those marked light red do not exists or have not been calculated.

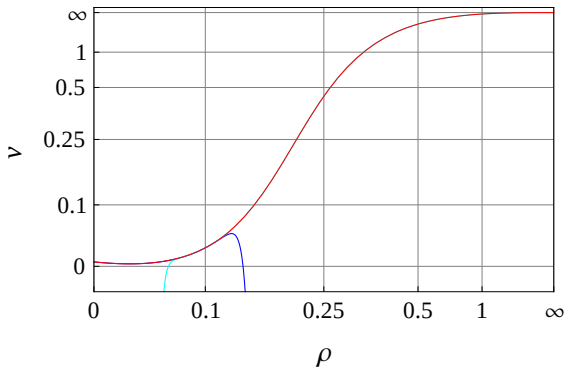

Fig. 18: The $[16/13]_6$ approximant (red) compared to the small field (blue) and large field (cyan) truncated series with $n_{\text{trunc}} = 25$ and $N_{\text{trunc}} = 25$ on the whole physical domain.

The lowest order expression with $\Delta_{(0,\infty)} < 10^{-7}$ is the $[11/8]_1$ approximant, which has $\Delta_{(0,\infty)} = 4.25(2) \times 10^{-8}$. This result is not beaten by any of the [12/9] or [13/10] terms.

Of all approximations we considered, the one with the minimum total deviation is the $[16/13]_6$ expression ($r = 9$, $R = 21$), for which we found $\Delta_{(0,\infty)} = 1.84(2) \times 10^{-8}$. This is one order of magnitude better than the combined small and large field series expansions connected at $\rho = 0.1$. More importantly, it is a single approximation to the average potential that is analytic in the whole physical domain. We plotted it on a global scale along with the small and large field series in Figure 18.

It should be noted that there are more expressions with similar accuracies among the [14/11] through [17/14] approximants. In each of these classes we find at least one choice for s such that $\Delta_{(0,\infty)} < 2 \times 10^{-8}$. The above quoted rule of thumb that the optimum weight lies in the range $0 < s < \frac{M+N}{4}$ is confirmed here.

At higher orders, our methods to evaluate $\beta(v)$ for a certain value of the field ρ turn out to be numerically unstable. We plotted this flow for the best approximants of the [13/10] and [16/13] classes in Figure 19. Starting from order [15/12], some of these graphs showed random jumps, hinting at problems with the numerics again. For the cases displayed in the figure, however, it can be seen

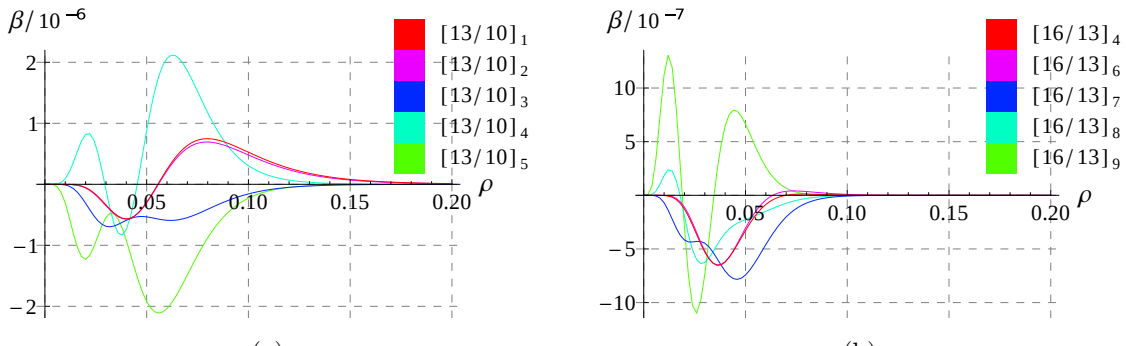

(a) (b)

Fig. 19: Flow $\beta(v)$ of the best approximants of the (a) [13/10] and (b) [16/13] classes as a function of ρ. The deviation from the fixed point solution is maximum around $\rho \approx 0.05$.

that the deviation is zero in the vicinity of the origin, then the approximants drift away from the fixed point solution, but the deviation falls off quickly again and becomes vanishingly small at $\rho \simeq 0.2$ in case of the [13/10] and at $\rho \simeq 0.1$ in case of the [16/13] terms.

Comparing to the distribution of poles and zeros in Figure 16, we see that for the approximants whose flow is shown in Figure 19(a), most of the poles of these approximants (the greenish ones in Figure 16) are located in the region $|\rho| = 0.02 \ldots 0.08$, which is where the deviation is largest.

Finally, it should be mentioned that all approximants show relatively large deviations at the location of the potential minimum at $\rho \approx 0.03$. Although we were able to approximate the potential by reasonably accurate expressions, this means that the minimum, being the "most interesting" point of the potential from a physical point of view, is not recovered as well as desired. We shall continue with a more thorough examiniation of physical properties and the extent to which they are preserved by these approximations in the next section.

3 Critical Exponents

In the following, we shall investigate the behavior of the average potential in the vicinity of the Wilson-Fisher fixed point. We will be able to extract *critical exponents* of the theory, which are a fundamental property of the physical system. It is this context where the relation between quantum and statistical physics is most striking. In particular, and in contrast to previous results, these critical exponents do not depend on the regulator chosen in the definition of the interpolating effective action [19]. They emerge from the eigenvalues obtained by a stability analysis of the fixed point and can be related to the behavior of a statistical system near a second-order phase transition [10, 27, 35, 45]. Most importantly, they allow to compare theory and experiment [45].

3.1 Stability Matrix

We consider for now an arbitrary expansion of the effective average potential v_k in terms of a set of coupling constants $\boldsymbol{c} = (c_0, c_1, \ldots)$. We assume that the flow equation for the potential has been reduced to a coupled set of flow equations for the couplings like in (2.4),

$$\partial_t c_m = \beta_m(\boldsymbol{c}) \qquad (m = 0, 1, \ldots)\,. \tag{3.1}$$

At the fixed point, characterized by $\boldsymbol{c}_\star$, we have of course $\beta_m(\boldsymbol{c}_\star) = 0$ for all m. We now expand (3.1) around the fixed point, letting $c_m = c_{\star m} + \delta c_m$. On the left-hand side, we find

$$\partial_t c_m = \partial_t c_{\star m} + \partial_t \delta c_m = \partial_t \delta c_m\,,$$

and on the right-hand side we expand β_m in powers of $\boldsymbol{\delta c}$:

$$\beta_m(\boldsymbol{c}) = \beta_m(\boldsymbol{c}_\star) + \sum_n \left.\frac{\partial \beta_m}{\partial c_n}\right|_{\boldsymbol{c}=\boldsymbol{c}_\star} \delta c_n + \frac{1}{2!} \sum_{n_1,n_2} \left.\frac{\partial^2 \beta_m}{\partial c_{n_1} \partial c_{n_2}}\right|_{\boldsymbol{c}=\boldsymbol{c}_\star} \delta c_{n_1} \delta c_{n_2} + \ldots$$

To leading order in $\boldsymbol{\delta c}$, we thus obtain the relation

$$\partial_t \delta c_m = \sum_n \left.\frac{\partial \beta_m}{\partial c_n}\right|_{\boldsymbol{c}=\boldsymbol{c}_\star} \delta c_n\,, \tag{3.2}$$

which we can be written

$$\partial_t \boldsymbol{\delta c} = S \boldsymbol{\delta c}\,, \qquad S_{mn} = \left.\frac{\partial \beta_m}{\partial c_n}\right|_{\boldsymbol{c}=\boldsymbol{c}_\star}\,. \tag{3.3}$$

Although it may not be the case in general, we now assume that the *stability matrix* S can be characterized by its eigenvalues $\omega_1, \omega_2, \ldots$, and $\boldsymbol{V}_1, \boldsymbol{V}_2, \ldots$ shall be the corresponding eigenvectors. The solution to this equation then takes the form

$$\boldsymbol{\delta c} = \sum_m \varepsilon_m \boldsymbol{V}_m \mathrm{e}^{\omega_m t} = \sum_m \varepsilon_m \boldsymbol{V}_m \left(\frac{k}{\Lambda}\right)^{\omega_m} \qquad (\varepsilon_m = \text{const})\,. \tag{3.4}$$

Bearing in mind the definition of the RG time $t = \ln(k/\Lambda)$ and the fact that the RG flow runs from $k = \Lambda$ to $k = 0$ (from $t = 0$ to $t = -\infty$), we understand that as the RG time progresses the solution approaches the fixed point along the eigendirections belonging to eigenvalues with a positive real part whereas it drifts away from the fixed point for eigenvalues with a negative real part. The $\boldsymbol{V}_m$ of the former class are called *irrelevant*, the ones of the latter class *relevant*, and those with vanishing coefficient to first order *marginal* operators [20, pp. 13-14]. Hence only relevant and potentially marginal operators affect the macroscopic behavior, and consequently the number of negative eigenvalues determines the system's number of degrees of freedom.

The eigenvalues describe a power-law scaling relation of the couplings in the vicinity of the fixed point. Borrowing from statistical physics, they are referred to as *critical exponents*. Indeed, in statistical

field theory, the most relevant eigenvalue ω_1 is related to the exponent ν of the correlation length ξ via $\nu = -1/\omega_1$, and subleading eigenvalues mediate corrections [10, 24]. The correlation length itself describes the asymptotic behavior of the two-point function. In the vicinity of the fixed point (i.e. the critical point), the correlation length scales like $\xi \sim |\tau|^{-\nu}$ where $\tau = (T - T_C)/T_C$ is the reduced temperature. In case of the small field series, for example, it may be identified with the parameter $\Delta\lambda = \lambda - \lambda_\star$ (or any other coupling used to fine-tune to the fixed point). In this way, field-theoretic results can be tested experimentally on real-world systems.

Critical exponents of the Wilson-Fisher fixed point in $O(1)$ scalar field theory have been computed by various methods in the past. It is found that there is only one relevant eigendirection with an eigenvalue ω_1 usually quoted $\nu = -1/\omega_1$. Its value is reported as $\nu = 0.6304(13)$ by a perturbative expansion of ϕ^4 theory in [46] or $\nu = 0.6294(2)$ by Monte-Carlo methods in [47]. A comprehensive collection of both theoretical and experimental results is given in [45], and it is confirmed that theoretical predictions agree with experiment. Correspondingly, $\omega_1 \simeq -1.58$ is expected as the leading contribution to the spectrum of the stability matrix that we shall probe now for the various approximation schemes we employed.

3.2 Small Field Series

For the weak field solution calculated in Section 2.1, we have the β functions at hand by (2.3). It is straightforward to set up the stability matrix S for a given truncation n_{trunc} and calculate its eigenvalues. Note that this way, we only consider perturbations consistent with $\mathbb{Z}_2$ symmetry.

Independent of the truncation n_{trunc}, all eigenvalues are found to be real, and two of them are negative. Furthermore, the smallest eigenvalue is $\omega_0 = -3$ regardless of n_{trunc}. Since the corresponding eigenvector is $\boldsymbol{V}_0 = (1, 0, 0, \ldots)$, we understand that it is directly related to the coefficient c_0, which is just a shift of the vacuum energy. But since the reference point for measuring energies is arbitrary, we will exclude the eigenvalue ω_0 from our discussion from now on.

Thus the only relevant degree of freedom links to the remaining negative eigenvalue ω_1. Its dependence upon the truncation is plotted in the top panel of Figure 20(a). We see that it settles down quickly to a value of $\omega_1 = -1.5394\ldots$ corresponding to a critical exponent $\nu = 0.6495\ldots$ which conforms with the results obtained in [26, 48]. The deviation from the above quoted values is caused by the approximative character of the effective action. Within the framework of the LPA, our value can be considered to reflect the standard result [26,43,48]. The two next smallest eigenvalues are plotted in the subsequent panels of Figure 20(a). Their values are determined as $\omega_2 = 0.655\ldots$ and $\omega_3 = 3.180\ldots$, respectively.

We also note that the eigenvalues and thus the critical exponent ν crucially depend on the mass parameter λ. This is illustrated in Figure 21 where we varied λ in the interval $(-0.3, -0.1)$ and calculated the first three eigenvalues. Their variation with λ is quite noticeable, which is expected seeing as a wrong choice of λ means the Wilson-Fisher fixed point is missed. The result is compared to the high-accuracy calculations performed in [48]. We see that at the scale considered, the curves pass right through the intersection point of the exponents calculated there and our choice of $\lambda_\star$.

3.3 Critical Exponents from Padé Approximants

After having computed a global approximation to the Wilson-Fisher fixed point potential in Section 2.3, we would like to investigate how much of the physical information about the local behavior of the RG flow around the fixed point these expressions still contain. Therefore, we shall derive flow equations for the generalized Padé couplings $a_0, \ldots, a_M, b_1, \ldots, b_N$.

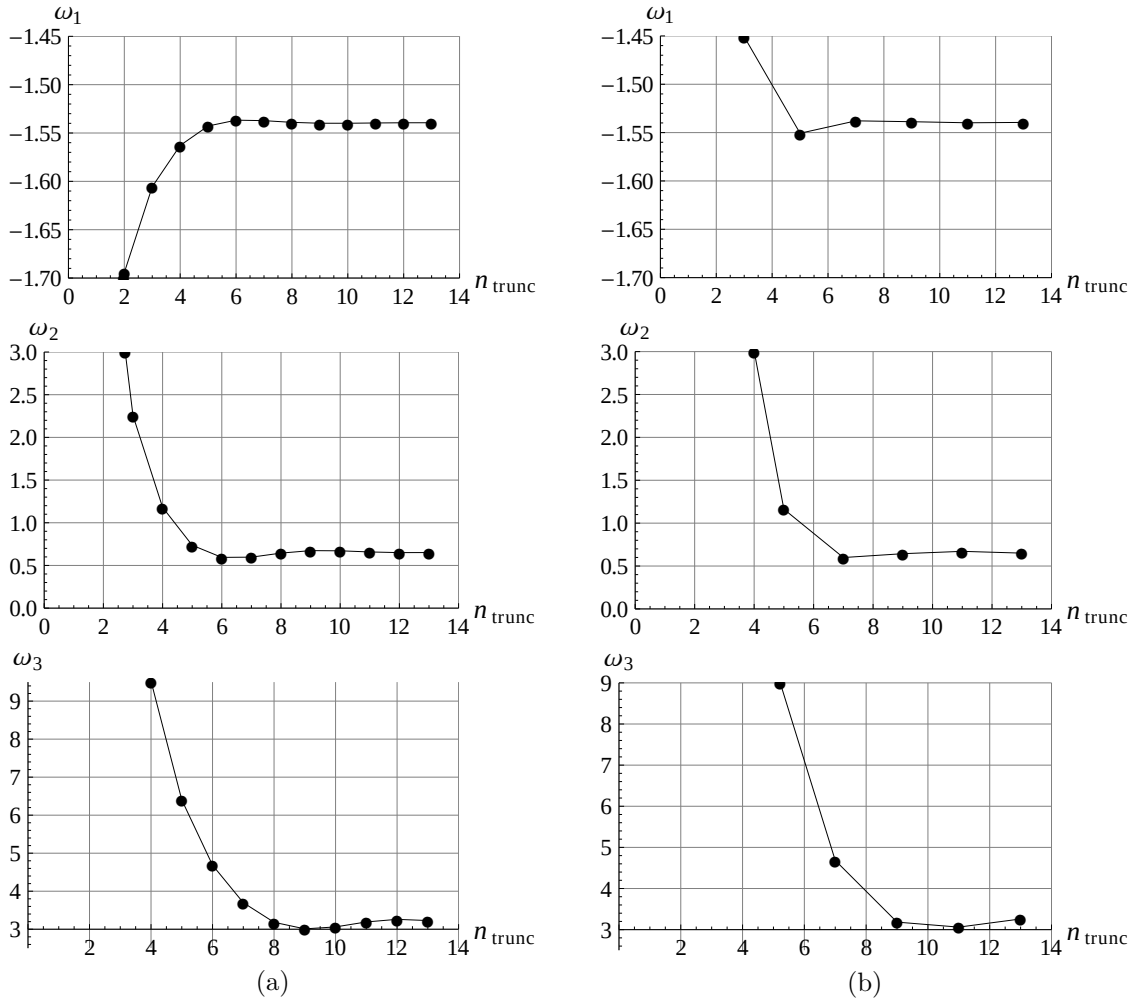

Fig. 20: Dependence of the three smallest eigenvalues ω_1, ω_2, ω_3 of the stability matrix for different approximation schemes upon the truncation n_{trunc}. (a) Stability matrix obtained from the small field power series couplings c_0, c_1, ... (b) Stability matrix obtained from the small field Padé approximant couplings $a_1, \ldots, a_M$, $b_1, \ldots, b_N$ where $M - N = 3$ and $M + N = n_{\mathrm{trunc}}$.

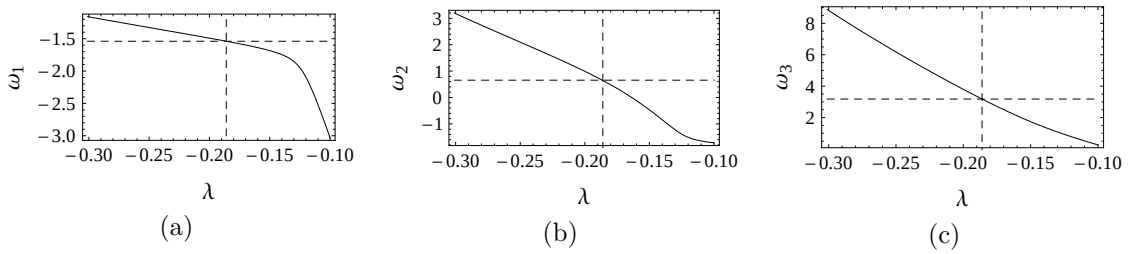

Fig. 21: Dependence of the eigenvalues (a) ω_1, (b) ω_2, and (c) ω_3 upon the mass parameter λ. The horizontal lines mark the LPA values taken from [48]: $\omega_1 = -1.539\,499$, $\omega_2 = 0.655\,746$, $\omega_3 = 3.180\,007$ (rounded to 6 decimal places). The vertical lines indicate the previously determined value of $\lambda_\star = -0.186\,064\,250$.

The relation between the Padé couplings and the couplings $c_0, \ldots, c_{n_{\text{trunc}}}$ for fixed truncation $n_{\text{trunc}} = M + N$ is given by (see also Appendix B)

$$\begin{pmatrix} 1 & 0 & 0 & & \cdots & & 0 \\ b_1 & 1 & 0 & & \cdots & & 0 \\ \vdots & b_1 & 1 & & & & \\ b_N & \vdots & b_1 & \ddots & & & \vdots \\ 0 & & & \ddots & & & \\ \vdots & & & & & 1 & 0 \\ 0 & & & & & b_1 & 1 \end{pmatrix} \begin{pmatrix} c_0 \\ c_1 \\ c_2 \\ \\ \\ \vdots \\ \\ \\ c_{n_{\text{trunc}}} \end{pmatrix} = \begin{pmatrix} a_0 \\ a_1 \\ \\ \vdots \\ \\ a_M \\ 0 \\ \vdots \\ 0 \end{pmatrix} \qquad \Leftrightarrow: \qquad B\boldsymbol{c} = \begin{pmatrix} \boldsymbol{a} \\ \boldsymbol{0} \end{pmatrix} .$$

Multiplying by B^{-1} from the left, we obtain

$$\begin{pmatrix} c_0 \\ c_1 \\ \\ \vdots \\ \\ c_{n_{\text{trunc}}} \end{pmatrix} = \begin{pmatrix} \tilde{b}_0 & 0 & \cdots & & 0 \\ \tilde{b}_1 & \tilde{b}_0 & \ddots & & \\ \vdots & \tilde{b}_1 & \ddots & & \vdots \\ & \vdots & \ddots & \tilde{b}_0 & 0 \\ \tilde{b}_{M+N} & & & \tilde{b}_1 & \tilde{b}_0 \end{pmatrix} \begin{pmatrix} a_0 \\ \vdots \\ a_M \\ 0 \\ \vdots \\ 0 \end{pmatrix}, \tag{3.5}$$

where $\tilde{b}_0 = 1$, $\tilde{b}_i = -\sum_{k=0}^{i-1} \tilde{b}_k b_{i-k}$. This is just a coordinate transformation in the space of coupling constants: The power series couplings $\boldsymbol{c} = (c_0, \ldots, c_{n_{\text{trunc}}})$ are expressed in terms of the Padé couplings $(a_0, \ldots, a_M, b_1, \ldots, b_N)$, which we shall collectively denote by $\hat{\boldsymbol{c}} = (\boldsymbol{a}, \boldsymbol{b})$. Note that this transformation is nonlinear; for example, $c_1 = a_1 - a_0 b_1$. Given the flow of the couplings $\boldsymbol{c}$ via the β functions $\boldsymbol{\beta} = (\beta_0, \ldots, \beta_{n_{\text{trunc}}})$ as before, we would like to find the flow of the Padé couplings,

$$\hat{\beta}_m(\hat{\boldsymbol{c}}) \equiv \partial_t \hat{c}_m = \sum_n \frac{\partial \hat{c}_m}{\partial c_n} \frac{\partial c_n}{\partial t} = \sum_n \frac{\partial \hat{c}_m}{\partial c_n} \beta_n(\boldsymbol{c}(\hat{\boldsymbol{c}})) . \tag{3.6}$$

The matrix $\partial \hat{c}_m / \partial c_n$ is the inverse of the Jacobian $J_{mn} = \partial c_m / \partial \hat{c}_n$ of the transformation (3.5). From the Padé β functions $\hat{\beta}_{a_i}$, $\hat{\beta}_{b_j}$, we can again determine the stability matrix $\hat{S}$ with components

$$\hat{S}_{mn} = \left. \frac{\partial \hat{\beta}_m}{\partial \hat{c}_n} \right|_{\hat{\boldsymbol{c}} = \hat{\boldsymbol{c}}_\star} = \left. \sum_{i,j} \left[\frac{\partial^2 \hat{c}_m}{\partial c_i \partial c_j} \frac{\partial c_j}{\partial \hat{c}_n} \beta_i + \frac{\partial \hat{c}_m}{\partial c_i} \frac{\partial \beta_i}{\partial c_j} \frac{\partial c_j}{\partial \hat{c}_n} \right] \right|_{\hat{\boldsymbol{c}} = \hat{\boldsymbol{c}}_\star} \tag{3.7}$$

$$= \left. \sum_{i,j} \frac{\partial \hat{c}_m}{\partial c_i} \frac{\partial \beta_i}{\partial c_j} \frac{\partial c_j}{\partial \hat{c}_n} \right|_{\hat{\boldsymbol{c}} = \hat{\boldsymbol{c}}_\star} \tag{3.8}$$

because $\beta_i(\boldsymbol{c}_\star) = 0$ by definition of the fixed point. Altogether,

$$\hat{\boldsymbol{\beta}} = J^{-1} \boldsymbol{\beta} \quad \text{and} \quad \hat{S} = J^{-1} S J ; \tag{3.9}$$

the matrices S and $\hat{S}$ are related by a similarity transform and thus have the same eigenvalues.

However, there remains a subtlety to this method due to the finite truncation. In general, the function β_n depends on all coefficients c_0 through c_{n+1}; in particular, $\beta_{n_{\text{trunc}}}$ depends on $c_{n_{\text{trunc}}+1}$. Usually, we set $c_{n_{\text{trunc}}+1} \equiv 0$ in $\beta_{n_{\text{trunc}}}$. For the power series expansion, this has the effect that $\beta_{n_{\text{trunc}}}(\boldsymbol{c}_\star) \neq 0$, but all other β_n are still annihalted by the fixed point solution. Therefore, the impact on the stability matrix and its spectrum is relatively small. In the case of Padé parametrization, unfortunately, the dependence upon $c_{n_{\text{trunc}}+1}$ becomes manifest in all couplings except a_0, and setting $c_{n_{\text{trunc}}+1} \equiv 0$ in all terms messes up the stability matrix because we have $\hat{\beta}_n(\hat{\boldsymbol{c}}) \neq 0$ for all $n \geq 1$. In particular,

the step from (3.7) to (3.8) is no longer valid. Hence S and $\hat{S}$ are no longer related by a similarity transformation, so that the spectrum is not preserved.

In order to be able to calculate critical exponents from Padé couplings nonetheless, we modify the transformation of β functions (3.6) slightly and set $\beta_{n_{\text{trunc}}} \equiv 0$, effectively reducing the order of truncation in the flow of the couplings. Consequently, all Padé couplings satisfy their individual flow equations again: $\hat{\beta}_n(\hat{\boldsymbol{c}}_\star) = 0$ for all $n = 0, \dots, M+N$.

Note that a similar effect could have been achieved by substituting the known value of $c_{n_{\text{trunc}}+1}$ from the next order of the truncation into $\beta_{n_{\text{trunc}}}$. However, this method is more artificial in the sense that it introduces $c_{n_{\text{trunc}}+1}$ as a random parameter that is unrelated to the Padé approximant at this order. In particular, the $(n_{\text{trunc}}+1)$-th coefficient in a Taylor series expansion of the $[M/N]$ approximant is generally different from $c_{n_{\text{trunc}}+1}$.

Having restored the fixed point condition for the Padé couplings, we can compute $\hat{S}$ from these modified $\hat{\beta}$ functions in the usual way, $\hat{S}_{mn} = \partial\hat{\beta}_m/\partial\hat{c}_n|_{\hat{\boldsymbol{c}}=\hat{\boldsymbol{c}}_\star}$, and determine its eigenvalues.

To show the validity of this method, we calculate the critical exponents obtained from the small field series Padé approximants and compare them with those obtained from the series directly choosing $M - N = 3$ such that the controlling factor is ρ^3 as $\rho \to \infty$. We first notice that—like in the previous case—all eigenvalues are real. Furthermore, the smallest eigenvalue turns out to be $\hat{\omega}_0 = -3$, which we will ignore as before, and there is one more negative eigenvalue converging to $\hat{\omega}_1 = -1.539\ldots$, too. Next in order we find $\hat{\omega} = 0$, again regardless of truncation. This is an artefact of the approximations made during the coupling transformation, to be traced back to setting $\beta_{n_{\text{trunc}}} \equiv 0$ in (3.6); we will therefore ignore this eigenvalue as well.

For comparison, the dependence of the eigenvalues as calculated from the flow of the Padé approximants by the above method upon the order of truncation is plotted in Figure 20(b). All in all, it can be seen that the stability matrix obtained from the Padé couplings exhibits the same spectrum as does the one obtained from the ordinary power series expansion, although convergence is slower due to the approximations made. Also, the computing time is considerably larger in the Padé case because the $\hat{\beta}$ functions are more complicated than their power series counterparts.

3.4 Large Field Series

Unfortunately, the stability matrix method does not work in the large-field case due to the fact that its spectrum is entirely controlled by the scaling part of the fixed point equation. Let us consider again an inverse power series like (2.19) with couplings C_{n_0}, C_{n_0+1}, …, $C_{N_{\text{trunc}}}$ starting with some arbitrary order $n_0 \leq -3$. We would like to investigate the form of the corresponding β functions. The contribution of the scaling part is trivial,

$$\beta_n(\boldsymbol{C}) = -(n+3)C_n + \dots . \tag{3.10}$$

The leading order of the coarse-graining part is proportional to ρ^{n_0+1}/C_{n_0} as can be seen by plugging the power series into the right-hand side of (2.1). Consequently, the first β function affected by this part is $\beta_{-(n_0+1)}$. But this implies that the stability matrix $\partial\beta_m/\partial C_n$ is triangular, and the diagonal elements—corresponding to the eigenvalues in this case—are solely determined by the scaling part (3.10). More precisely, we find the eigenvalues $-(n_0+3)$, $-(n_0+4)$, …, $-(n_0+3+N_{\text{trunc}})$.

Since this simple approach does not function, we go back to the flow equation for the average potential (1.24) and add a small perturbation similar to (3.4) to the fixed point solution directly:

$$v_k(\rho) = v_\star(\rho) + \varepsilon h(\rho)\mathrm{e}^{\omega t}\,, \quad \varepsilon \ll 1\,, \tag{3.11}$$

where ω is the eigenvalue we are looking for. Plugging this into (1.24) leads to the following differential equation for h:

$$-(\omega+3)h + \rho h' = \frac{1}{6\pi^2}\frac{h' + 2\rho h''}{\left(1 + v_\star' + 2\rho v_\star''\right)^2}\,. \tag{3.12}$$

In order to determine the eigenvalues ω, we have to solve (3.12) along with some boundary condition. The idea is similar to the procedure of Bridle, Dietz, and Morris [43] although they start from (1.22), using the classical field $\tilde{\phi} = \sqrt{2\rho}$ instead, and integrate the corresponding equation for the perturbation numerically, in contrast to our intention here.

To solve (3.12), we use the method of dominant balance similar to how it was described in Section 2.2.1 in order to find a series representation of its solution. To leading order, neglecting the right-hand side, we find $h_{(0)}(\rho) = \rho^{\omega+3}$ where we set the arbitrary normalization constant to unity. Subsequent orders are obtained by substituting the previous result into the right-hand side and expanding to leading order in a Taylor series at infinity. This way, we calculated

$$\begin{aligned} h(\rho) &= \rho^{\omega+3} - \frac{(\omega+3)(2\omega+5)}{6750\pi^2 A_\star^2}\rho^{\omega-2} + \frac{(\omega+3)(2\omega+5)}{70\,875\pi^2 A_\star^3}\rho^{\omega-4} + \dots \\ &=: \rho^\omega h_P(\rho)\,, \end{aligned} \tag{3.13}$$

where we separated the polynomial (or rather integer-power) part

$$h_P(\rho) = \rho^3 + (\omega+3)(2\omega+5)\left[-\frac{1}{6750\pi^2 A_\star^2\rho^2} + \frac{1}{70\,875\pi^2 A_\star^3\rho^4} + \dots\right]. \tag{3.14}$$

Instead of a numerical integration, we shall approximate the perturbation by a Padé function again. Since we can only treat uniformly increasing powers by this method, we restrict ourselves to the computation of an approximation to the polynomial part h_P, such that $h(\rho) \approx \rho^\omega\, \mathcal{P}_{[M/N]} h_P(\rho)$.

Let us now turn our attention to finding an appropriate boundary condition so as to quantize the eigenvalue spectrum. One option, employed in [43], is to classify the perturbations as even or odd functions of the field $\tilde{\phi}$. This should be done by adding a perturbation $g = g(\tilde{\phi})$ to the fixed point solution $u_\star(\tilde{\phi}) = v_\star(\frac{1}{2}\tilde{\phi}^2)$ and substituting into (1.22). Thereafter, one can impose the boundary conditions

$$g(0) = 0 \qquad \text{and} \qquad g'(0) = 0 \tag{3.15}$$

in order to find odd and even perturbations, respectively. Although we could have started from (1.22) working with the field $\tilde{\phi}$, too, this would not have yielded any progress combined with the Padé method because we would not have been able to use conditions (3.15) anyway. The reason is that this way we obtain a series similar to (3.13), where we have to split off the polynomial part as before, $g(\tilde{\phi}) = \tilde{\phi}^{2\omega} g_P(\tilde{\phi})$ in order to be able to compute Padé approximants. But since the Padé expressions are regular at the origin by definition, conditions (3.15) are satisfied for any $\omega > 0$ or $\omega > 1$, respectively.

Another approach to deal with the parity conditions would be to impose them on the polynomial part or its Padé approximant, respectively. Although it is *a priori* unknown whether $\tilde{\phi}^{2\omega}$ is even or odd or whether this question is meaningful at all, we could enforce the condition on g_P and compute the corresponding eigenvalues ω. These would then determine the parity of $\tilde{\phi}^{2\omega}$ and thus of the whole expression $g(\tilde{\phi}) = \tilde{\phi}^{2\omega} g_P(\tilde{\phi})$. The reason why this does not work in this case, either, is that the series representation of g_P is already an even function of $\tilde{\phi}$ and so is its Padé approximant as a result.

We shall therefore use a different quantization condition called the *Padé-Hankel* method. It is described, for example, in [40] or [15], and we had mentioned it in Section 2.1.5 as a way to estimate the mass parameter λ of the small field series (see also Appendix B.3).

By construction, the first $M+N+1$ terms of a power series expansion of the $[M/N]$ Padé approximant match with those of the approximated function h. The idea of the Padé-Hankel method is to estimate the remaining parameter ω, by requiring that this matching condition hold for the next-order coefficient, too. Adopting this method to a sequence of Padé approximants of increasing order, we hope to find a converging behavior leading to the eigenvalues sought.

The method has proven successful in various instances; examples can be found in [15, 40] as well. A particular motivation may be that it provides another way to establish an accurate guess of the mass

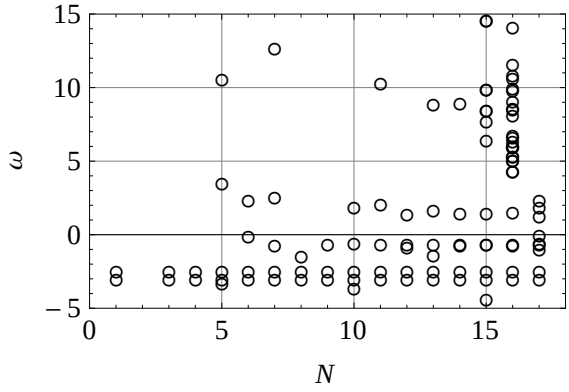

Fig. 22: Real solutions ω in the range $(-5, 15)$ of the Padé-Hankel condition imposed on the $[N+3/N]$ approximants.

parameter λ of the small field series, a fact that is worked out in Appendix B.3. We note, though, that the free parameter A of the large field series was not extractable by this procedure.

There are two eigenvalues that can in fact be read off equations (3.12) and (3.14) directly. The first one is the well-known $\omega = -3$ solution corresponding to $h = \text{const}$ that we had already encountered in the previous sections. The second one is $\omega = -\frac{5}{2}$, and the reason why we have not found it before is that it is an odd perturbation: It is linked to the operator $h(\rho) = \sqrt{\rho} \sim \tilde{\phi}$, which may be present, for instance, when coupling to an external source, and clearly breaks $\mathbb{Z}_2$ invariance.

These two solutions are also manifest in Figure 22 where we plotted the values ω that satisfy the Padé-Hankel condition for the $[N+3/N]$ approximants to h_P up to order $N = 18$. Frankly, these are the only two values showing a definite converging behavior for they are present at every order. It should be mentioned, too, that the picture of Figure 22 is not complete. On the one hand, we ignored all complex-valued solutions. On the other hand, the figure shows only values between -5 and 15, but some may lie to either side of the interval. Nevertheless, the selected range is the region where the solutions concentrate.

Another accumulation point is at $\omega \approx -0.65$ where there are close-by solutions in every term starting from $N = 7$. In [43], another solution $\omega = -\frac{1}{2}$ is reported, although it is characterized as redundant there. It may or may not be associated with our finding.

On the contrary, opposing expectations from the previous sections, we cannot locate any clustering around $\omega \approx -1.5$. There are approximants such as $N = 8$ or $N = 13$ for which a solution in this region exists, but their appearance seems to be rather random. Instead, the next aggregation is found in the irrelevant regime at $\omega \approx +1.5$. In Section 3.2, the first two positive eigenvalues found were $\omega_2 \approx 0.66$ and $\omega_3 \approx 3.2$, so that the results here do not match apparently.

Curiously enough, our solutions $\omega \approx -0.65$ and $\omega \approx 1.5$ would comply with the expected values $\omega_1 \approx -1.5$ and $\omega_2 \approx 0.65$ if they were shifted by about 0.85, but this coincidence is merely a peculiarity. Although there surely remains an uncertainty associated with the parameter A, for instance, the error cannot be large enough to make up for the above deviation. As an example, we would need $A \simeq 20$ in order to move $\omega \approx -0.65$ to about -1.5. This is inacceptable, especially in view of the small deviation we obtained for $A_\star$ compared with [43].

We must therefore conclude that the spectrum of critical exponents linked to the Wilson-Fisher fixed point is not accessible from the large field series by our methods. It remains unclear whether this is a limitation of the methods or an intrinsic peculiarity of the series itself. On the one hand, the series' radius of convergence does not extend to the "critical region" around the vacuum expectation value, but on the other hand, its resummation by means of Padé approximants appeared to recover this neighborhood quite well.

Tab. 2: Spectrum of a selection of [6/3] approximants*

M	N	r	R	spectrum
6	3	10	0	-3, -1.538, 0, 6.438^{-1}, 3.183, 9.208, 2.242^{1}, 4.734^{1}, 9.247^{1}, 1.784^{2}
6	3	8	2	-3, -1.539, -1, 0, 0,5.989^{-1}, 4.683, 1.542^{1}, 3.932^{1}, 9.172^{1}
6	3	6	4	-3, -2, -1.579, -1,-2.478^{-1}, 0, 1.461, 9.732, 2.776^{1},1.711^{3}
6	3	4	6	-5, -4, -3, -3, -2, -1.450, -1, 0, 0, 4.851
6	3	2	8	-7, -6, -5, -4, -3, -3, -2, -1, 0, 0
6	3	0	10	-9, -8, -7, -6, -5, -4, -3, -2, -1, 0

3.5 Critical Information of the Global Approximation

In this final section, we would like to explore how much of the critical information we can restore from the two-point rational approximations calculated in Section 2.3 by the stability matrix method.

The first thing we note is that the $\hat{\beta}$ functions for the Padé coefficients, calculated above in Section 3.3, are not universal in the sense that they do not generally vanish for other weights (r, R) than the ones they were computed with. In other words, in Section 3.3 we transformed the small field series' β functions, corresponding to a weight of $r = M+N+1$, $R = 0$, into the functions $\hat{\beta}_m$ which described the flow of the couplings $a_0, \ldots, a_M, b_1, \ldots, b_N$, and we observed that, indeed, $\hat{\beta}_m(\hat{\boldsymbol{c}}) = 0$ for all m. But if we use these $\hat{\beta}$ functions to compute the flow of Padé coefficients from a different weight (r, R), we find that the individual components of the flow vector $\hat{\boldsymbol{\beta}}$ deviate tremendously from zero, although the total flow $\beta(\hat{v})$ where $\hat{v} = \hat{v}(\rho)$ is the rational Padé function may actually satisfy the fixed point condition better.

This may be surprising at first glance. After all, the structure of the Padé function and the role of the coefficients a_i and b_j is essentially the same for all weights (r, R) within a class of $[M/N]$ approximants. However, the transformation of β functions (3.6) makes use of the explicit form of the coupling transformation (3.5), and of course this differs for different weights.

Therefore, we are forced to calculate the $\hat{\beta}$ functions for each weight individually. The strategy is exactly the same as in Section 3.3, but we use the mixed coupling transformations (Appendix B.1.3) and the corresponding β functions from both series with the appropriate weight instead. As for the small field part, we set $\beta_{r-1} \equiv 0$ again in order to compensate for the extra coupling c_r not represented in the transformation. This way, all $\hat{\beta}_m$ vanish by virtue of the definition, and we are ready to evaluate the stability matrix. It should be noted, though, that we were not always able to verify $\hat{\beta}_m(\hat{\boldsymbol{c}}) = 0$ due to numerical instabilities (see also Appendix D).

Generally speaking, the expressions obtained for the $\hat{\beta}$ functions by this method become rather lengthy. In order that the actual calculation would not become useless due to numerical errors, it was crucial to simplify the terms as much as possible by means of *Mathematica*'s symbolic simplification procedures. This way, we established the stability matrix and computed its spectrum for all two-point Padé approximants with $M - N = 3$ up to order [6/3] and for most of the [7/4] approximants. The determined spectra are collected in Table 3 in Appendix D along with the respective fixed point deviations $\Delta_{(0,\infty)}$. An excerpt is presented in Table 2.

It can be seen that the two-point Padé spectrum is basically a mix of the small and large field spectra obtained by the stability matrix method that resembles the particular weight (r, R). The more terms of the small field series are included, the more critical exponents appear, whereas the large field terms only contribute the spurious negative integers we already found in Section 3.4.

Tables 2 and 3 reveal the hierarchy of eigenvalues again that was already observable in Section 3.2. With regard to the small field series, the first eigenvalue emerging ($r = 1$) is the artificial 0 that results

*The notation a^b is a shorthand for $a \times 10^b$. Decimal numbers are truncated, not rounded.

from setting $\beta_{r-1} \equiv 0$. The subsequent eigenvalues virtually come up in numerical order, starting with -3, -1.5, ...; this shows that the main contribution to the relevant operator comes from the low-order couplings c_1, c_2, etc. For the large field series, the spectrum starts with 0, -1, -2, ... as observed before.

Lastly, we note that the quality of the approximation in terms of the total deviation $\Delta_{(0,\infty)}$ is obviously not related to the amount of critical information extractable. Accuracy of the eigenvalues apparently does not improve for expressions with low overall deviation. Moreover, those approximants with a small total deviation tended to have $R > r$, but the exponents are better reflected by those with $r > R$.

All in all, no additional information is revealed by the Padé approximants using the stability matrix method. At the same time, no features of the individual spectra are lost, either. Considering the comparatively high demand of computing resources, the Padé method is not recommendable for the calculation of critical exponents. These are obtained more effectively from the β functions of the simple Taylor series, which have to be determined for the method used here anyway. To conclude, we can state that the Padé approximant *preserves* the critical information contained in the constituents that entered its construction.

Conclusions

In the framework of the functional renormalization group, this thesis presented an analytic approach to the effective average action characterizing the Wilson-Fisher fixed point in the three-dimensional $\mathbb{Z}_2$ model. Working in the local potential approximation, we aimed at an analytic expression to approximate the effective average potential. By probing its behavior in the vicinity of the fixed point, we went to find critical properties of theories constructed around it.

As a start, we expanded the solution of the fixed point equation in two limiting cases, namely for small values of the field around the origin and for large field values at infinity. In both cases, a recurrance relation for the series' coefficients was derived with one free parameter to be tuned to the Wilson-Fisher fixed point.

For the small field series, we determined the parameter by maximizing the radius of convergence. Investigating the sign structure of the series' coefficients, we revealed an interesting regularity which led to a refined definition of this parameter. It was found that the sign oscillates approximately every three coefficients, but a fourth term of equal sign turns up at about every 127th coefficient; this pattern was confirmed up to order 2000. From a fit to the series' coefficients, we estimated the radius of convergence to be about 0.0966.

Using the method of Padé approximants, we intended to extend convergence of the small field series. No significant improvement was achieved, but the distribution of poles and zeros unveiled some more properties of the fixed point potential. We found evidence for two branch points in the complex plane whose locations confirm the radius of convergence and additionally may be linked to the intruiging sign structure observed before.

In the large field case, no obvious choice of the free parameter was noticeable. However, we established that the large field series' domain of convergence reaches closely to that of the small field series. Therefore, we were able to determine the parameter's value characterizing the Wilson-Fisher fixed point by matching medium order truncations of the two series in a connecting interval. By combining certain truncations of the two series expansions, a global solution could be specified up to a total deviation of 4×10^{-7}.

As before, we computed various Padé approximants from the large field expansion as well. In this case, these expressions indeed allowed us to extend the solution to the whole positive real line, but the total deviation was about two orders of magnitude smaller than that of the combined series. Here, too, the poles and zeros of the Padé expressions suggested the existence of two branch points at similar locations as in the small field case. Nevertheless, more such points in the negative half-plane appeared which were not visible before.

Seeing as the Padé method had proven successful, we finally computed rational approximations to the average potential including terms from both limiting cases. This way, we were able to limit the total deviation on the whole positive real axis to less then 2×10^{-8}. Furthermore, we could observe the transformation of the singularity structure as a moving of the branch cut from infinity to the origin.

In order to extract critical exponents from our solutions, we set up the stability matrix and evaluated its spectrum for the various approximation schemes. The exponents computed from the small field series showed excellent agreement with those cited in the references. In the large field case, by contrast, the stability matrix method did not work because of degenerated β functions. In a second approach, we tried to work out the eigenvalues using the Padé-Hankel method, but the obtained spectrum agreed with previous results in trivial cases only and was distorted otherwise.

We could show, however, that the stability matrix method can be extended to Padé coupling constants by an appropriate transformation of the β functions. Calculating the eigenvalues for different orders and weights of the small and large field series, we established that the resulting spectrum is a combination of the individual contributions from the two limits. The overall finding was that the Padé functions did not disclose any new information, but all pieces contained in the contributing coefficients of the respective series were preserved.

A Sign Structure Diagrams

In the following diagrams, the sign of the first 200 coefficients of the small field series expansion is displayed as a function of the deviation $\Delta\lambda = \lambda - \lambda_\star$ from $\lambda_\star = -0.186\,064\,250(2)$. Every square corresponds to one pair $(\Delta\lambda, \mathrm{sgn}(c_n))$. Dark: $+1$; light: -1.

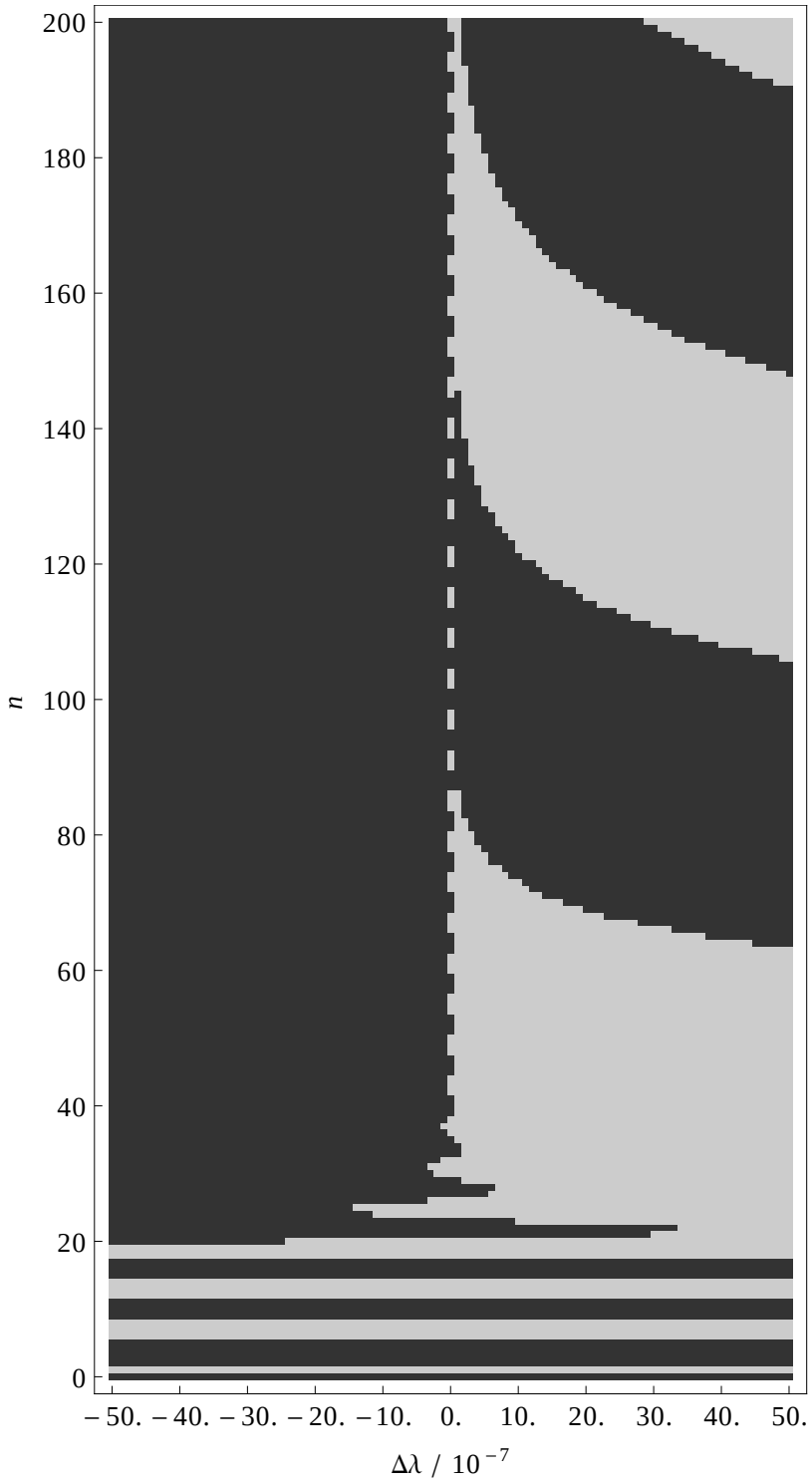

Fig. 23: Varying λ in the 7th digit, $\lambda_\star = -0.186064\underline{2}50$. The 'zipper' in the middle of the picture reflects the alternating structure at $\lambda = \lambda_\star$

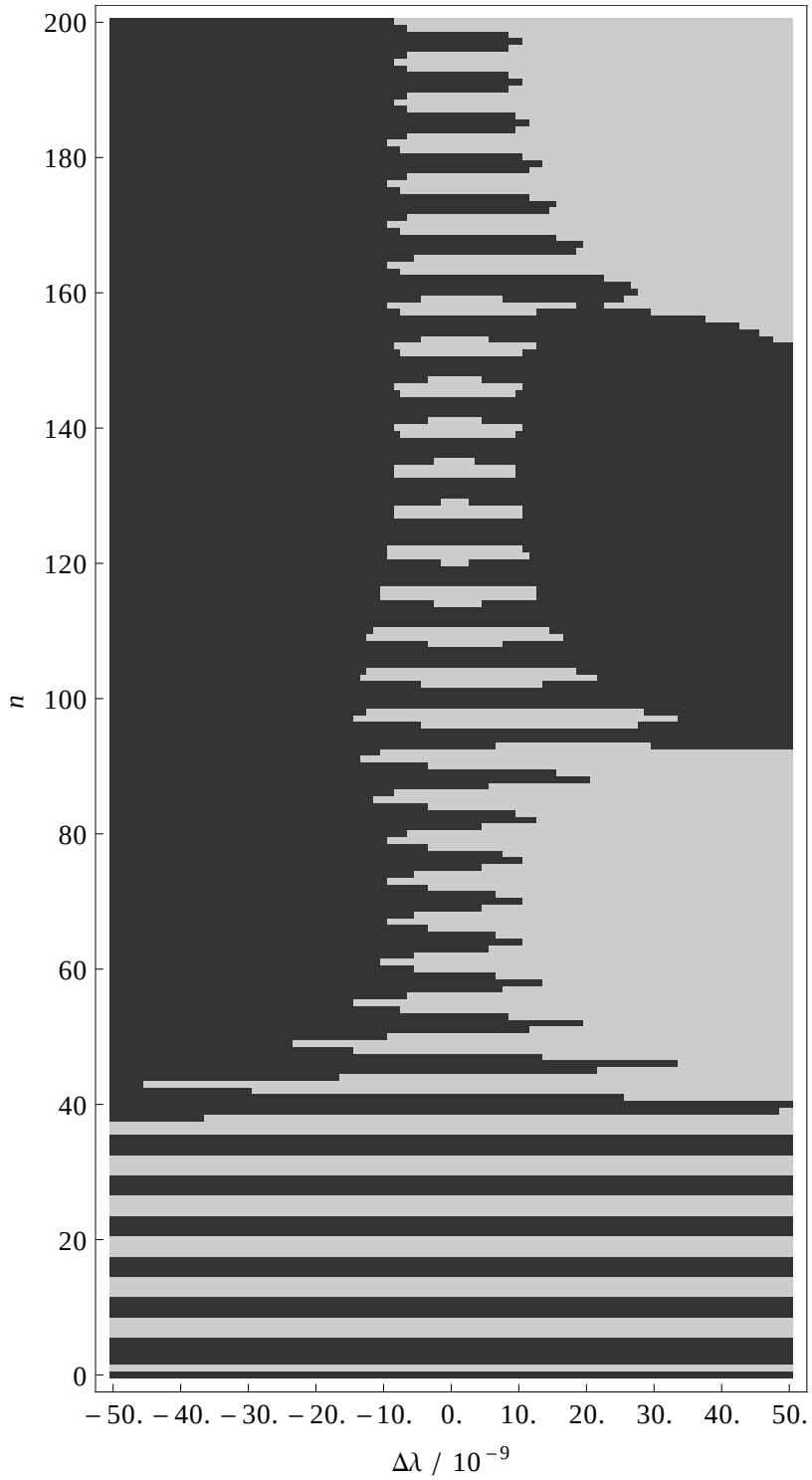

Fig. 24: Close-up of Figure 23, varying λ in the 9th digit, $\lambda_\star = -0.18606425\underline{\mathbf{0}}$. From the situation in the region from $n = 120$ to $n = 126$ we can limit the uncertainty of $\lambda_\star$ to ± 2 in the last digit in order to maintain the regular structure.

B Padé Approximants

Generally speaking, the convergence of power series is very limited. A Taylor series expansion of a function may only converge in a circle around the expansion point whose radius is determined by the location of the closest singularity or branch point from this expansion point in the complex plane. The idea of Padé approximants is to replace the approximating polynomial (i.e. the truncated power series) by a rational function. These rational expressions can include poles naturally and therefore have superior convergence properties. In addition, the locations of the poles may allow to recover information about singularities or branch points of the original function. The basic idea along with some example of accelerated convergence are presented in [35], an exhaustive treatment of the method and its applications is the book of Baker and Graves-Morris [36]. Many aspects of the analysis of special points in general and algebraic branch points in particular are explored in [37].

B.1 Calculation from Taylor-like Series

B.1.1 Expansion at 0

Consider a truncated power series,

$$v(\rho) = \sum_{n=0}^{n_{\text{trunc}}} c_n \rho^n \,. \tag{B.1}$$

We want to replace this expression by a quotient of polynomials of the form

$$\mathcal{P}_{[M/N]} v(\rho) = \frac{a_0 + a_1\rho + \ldots + a_M\rho^M}{1 + b_1\rho + \ldots ... + b_N\rho^N} \tag{B.2}$$

where $M + N = n_{\text{trunc}}$. The coefficients a_i, b_j are determined such that they coincide with the Taylor coefficients c_n up to the order of truncation, i.e. we set

$$\begin{aligned}
&\sum_{n=0}^{n_{\text{trunc}}} c_n\rho^n = \frac{a_0 + a_1\rho + \ldots + a_M\rho^M}{1 + b_1\rho + \ldots ... + b_N\rho^N} \\
\Leftrightarrow \quad &\left(\sum_{j=0}^{N} b_j\rho^j\right)\left(\sum_{n=0}^{n_{\text{trunc}}} c_n\rho^n\right) = \sum_{i=0}^{M} a_i\rho^i \qquad (b_0 = 1) \\
\Leftrightarrow \quad &\sum_{i=0}^{n_{\text{trunc}}+N} \rho^i \sum_{j=0}^{i} b_j c_{i-j} = \sum_{i=0}^{M} a_i\rho^i \,.
\end{aligned}$$

Thus, the a_i and b_j are determined from the system of $M + N + 1$ equations

$$\begin{aligned}
&\sum_{j=0}^{i} b_j c_{i-j} = a_i \quad \text{for} \quad i = 0, \ldots, M \\
\text{and} \quad &\sum_{j=0}^{i} b_j c_{i-j} = 0 \quad \text{for} \quad i = M+1, \ldots, n_{\text{trunc}}
\end{aligned} \tag{B.3}$$

or in matrix form:

$$\begin{pmatrix} 1 & 0 & 0 & & \cdots & & 0 \\ b_1 & 1 & 0 & & \cdots & & 0 \\ \vdots & b_1 & 1 & & & & \\ b_N & \vdots & b_1 & \ddots & & & \vdots \\ 0 & & & \ddots & & & \\ \vdots & & & & & 1 & 0 \\ 0 & & & & & b_1 & 1 \end{pmatrix} \begin{pmatrix} c_0 \\ c_1 \\ c_2 \\ \\ \\ \vdots \\ \\ \\ c_{n_{\text{trunc}}} \end{pmatrix} = \begin{pmatrix} a_0 \\ a_1 \\ \\ \vdots \\ \\ a_M \\ 0 \\ \vdots \\ 0 \end{pmatrix} . \tag{B.4}$$

This form is used in Section 3.3 because it emphasizes the character of a coordinate transformation between power series and Padé coefficients. However, to actually compute the a_i and b_j it is more convenient to write (B.3) in a slightly different form. First, consider the second set of equations involving only the b_j. They are obtained as the solution of the linear system of equations

$$\bar{C} \begin{pmatrix} b_1 \\ \vdots \\ b_N \end{pmatrix} = - \begin{pmatrix} c_{M+1} \\ \vdots \\ c_{M+N} \end{pmatrix} , \qquad \bar{C}_{ij} = c_{M+i-j} \, . \tag{B.5}$$

The a_i can then be computed by substituting these solutions into the first set of equations of (B.3),

$$a_i = \sum_{j=0}^{i} c_{i-j} b_j \, . \tag{B.6}$$

B.1.2 Expansion at ∞

We now start with an inverse power series

$$v(\rho) = \sum_{n=0}^{N_{\text{trunc}}} C_{J-n} \rho^{J-n} \, , \tag{B.7}$$

where we have incorporated a leading order behavior of ρ^J as $\rho \to \infty$. The Padé approximation takes the same form as in (2.12), but we require $M - N = J$. Equating the two expressions, multiplying by the denominator and comparing powers of ρ, we are left with

$$\begin{aligned} \sum_{j=0}^{N} b_j C_{i-j} &= a_i \quad \text{for} \quad i = 0, \ldots, M \\ \text{and} \quad \sum_{j=0}^{N} b_j C_{i-j} &= 0 \quad \text{for} \quad i = -1, -2, \ldots, -N \, . \end{aligned} \tag{B.8}$$

To minimize computation time, the b_j may be calculated as the solutions of the linear system of equations

$$\bar{C} \begin{pmatrix} b_1 \\ \vdots \\ b_N \end{pmatrix} = - \begin{pmatrix} C_{-1} \\ \vdots \\ C_{-N} \end{pmatrix} , \qquad \bar{C}_{ij} = C_{-i-j} \quad (i, j = 1, \ldots, N) \, , \tag{B.9}$$

from which the a_i can then be calculated directly similar to the previous case:

$$a_i = \sum_{j=0}^{N} C_{i-j} b_j \,. \tag{B.10}$$

Note, however, that the sums convoluting b_j and C_{i-j} now run 0 to N in contrast to the previous case where they would run from 0 to i.

B.1.3 Two-Point Approximation at 0 and ∞

In a final step, we would like to establish a single approximating Padé expression incorporating information from a function's expansions both at 0 and at infinity. The approximation is to match r orders of the small field and R orders of the large field series. That is, our starting point are the truncated series

$$v_S(\rho) = \sum_{n=0}^{r-1} c_n \rho^n \qquad \text{and} \qquad v_L(\rho) = \sum_{n=0}^{R-1} C_{J-n} \rho^{J-n} \quad (J = M - N) \,. \tag{B.11}$$

In order to obtain a well-defined solution, we require $M + N + 1 = r + R$. As in the previous cases, we equate the Padé ansatz with the two series expansions and compare coefficients in powers of ρ. However, we have to bear in mind the different truncations now. From the small field limit, we use the first r equations of

$$\begin{aligned} \sum_{j=0}^{i} b_j c_{i-j} &= a_i \,, \qquad i = 0, \ldots, M \,; \\ \sum_{j=0}^{i} b_j c_{i-j} &= 0 \,, \qquad i = M+1, \ldots, M+N \,, \end{aligned} \tag{B.12}$$

i.e. i technically runs from 0 to $r - 1$ only. In a similar manner, we take into account the first R equations of

$$\begin{aligned} \sum_{j=0}^{N} b_j C_{i-j} &= a_i \,, \qquad i = M, M-1, \ldots, 0 \,; \\ \sum_{j=0}^{N} b_j C_{i-j} &= 0 \,, \qquad i = -1, -2, \ldots, -N \,, \end{aligned} \tag{B.13}$$

such that i runs reversely from M to $M - R + 1$ in this case. In this way, we are left with $r + R = M + N + 1$ equations for the $M + N + 1$ coefficients a_i, b_j. Note that it is guaranteed that each coefficient appears in at least one of the equations. In particular, all a_i are present because i starts from 0 in the small field, but from M in the large field limit. Setting either $R = 0$ or $r = 0$, we retrieve the sets of equations of Sections B.1.1 or B.1.2, respectively.

B.2 Recovery of Special Points

In this section we give an empirical survey of how Padé approximants pick up singular points of the approximated function. The examples are chosen on the analogy of the structure that was found for the small field series in Section 2.1.5. To be precise, we placed the special points at $\rho = \mathrm{e}^{\pm \mathrm{i}\Omega}/\alpha$ in the complex ρ plane where $\alpha = 0.095$ and $\Omega = \frac{\pi}{3}$, close to the ones detected there. We then expanded the model function v around the origin and calculated Padé approximants from this series expansion.

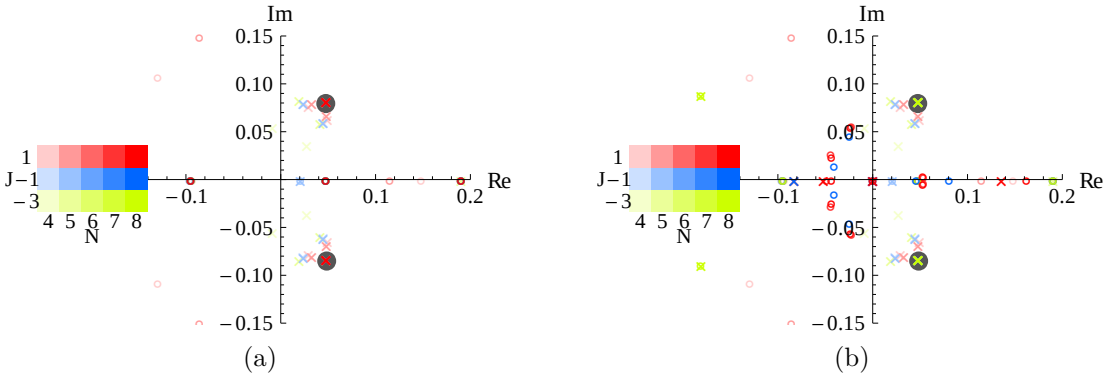

Fig. 25: Poles (×) and zeros (○) of $v(\rho) = \left(1 - \alpha e^{i\Omega}\rho\right)^{-3} + c.c.$ having *poles of order 3* at $\rho = e^{\pm i\Omega}/\alpha$; the pole is fully recovered by the [3/6] approximant and all higher order expressions in an exact calculation in (a). The poles are marked by filled gray circles. Blue and green crosses belonging to the $J = -3, -1$ approximants are hidden underneath the red ones. In (b), it can be seen that a numerical calculation of the Padé approximants produces spurious zeros. The extra poles lie outside the plotted region.

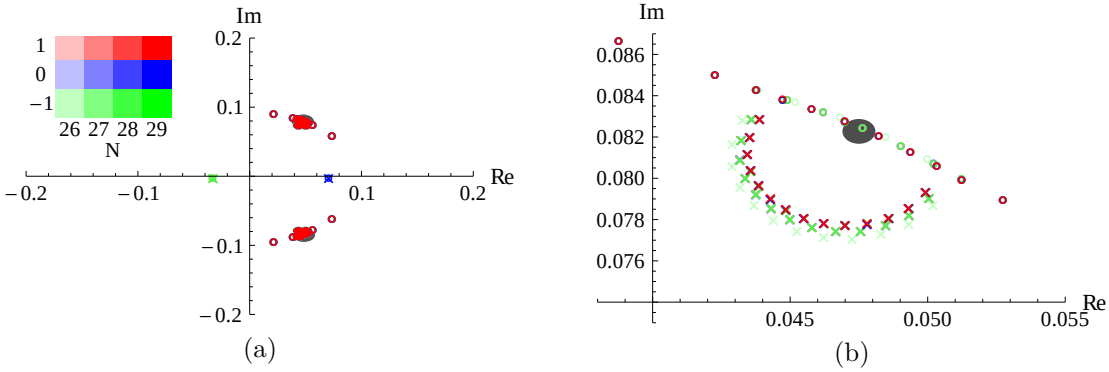

Fig. 26: Poles (×) and zeros (○) of $v(\rho) = \exp\left[1/\left(1 - \alpha e^{i\Omega}\rho\right)\right] + c.c.$ having *essential singularities* at $\rho = e^{\pm i\Omega}/\alpha$; in (a) it can be seen that the poles (and zeros) cluster around the singularity. The close-up (b) reveals that they do not hit the singularity but rather arrange in a (semi-)circle around it.

The first example is a multi-pole of order 3,

$$v(\rho) = \left(1 - \alpha e^{i\Omega}\rho\right)^{-3} + c.c.\,. \tag{B.14}$$

Poles and zeros of low-order Padé approximants are plotted in Figure 25. The function is fully recovered by the [3/6] expression, and all higher order approximants ($M \geq 3$, $N \geq 6$) reduce to the [3/6] approximant because the coefficients a_i and b_j vanish for $i > 3$, $j > 6$.

In the right panel of the figure, the poles and zeros of the exact same approximants are plotted, but here the Padé expressions were computed numerically with 80 digits precision. The figure reveals the discontinuity of the Padé operator for approximants with defects quite impressively. The approximants up to order [3/6] agree with the exact calculation, but for higher orders, the additional coefficients do not vanish and lead to spurious zeros and poles. The latter are not visible in the plot because they are located far away from the origin ($|\rho| \sim 1000$) and tend to drift towards infinity with increasing order.

As a second example, we placed essential singularities of the form

$$v(\rho) = \exp\left[1/\left(1 - \alpha e^{i\Omega}\rho\right)\right] + c.c. \tag{B.15}$$

at the same spots. The resulting pattern of Padé poles and zeros is shown in Figure 26. We see that almost all of them accumulate at the singular points. The detailed view in the right panel reveals that

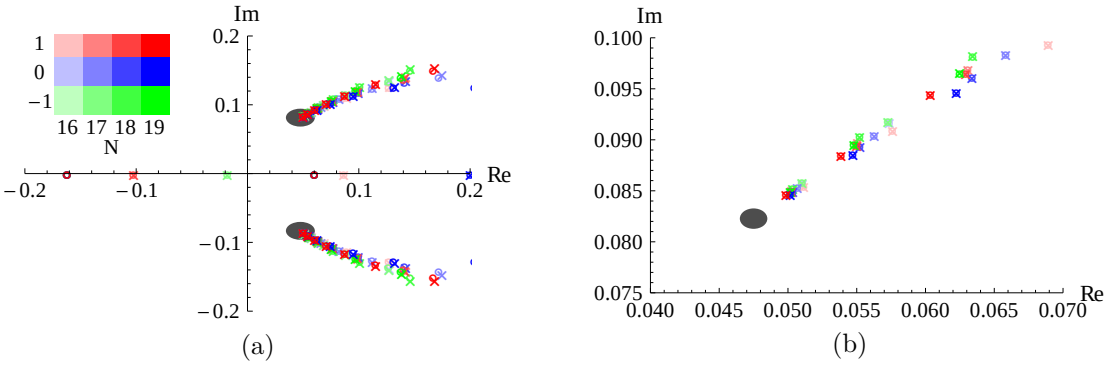

Fig. 27: Poles (×) and zeros (○) of $v(\rho) = \left(1 - \alpha e^{i\Omega}\rho\right)^{7/3} + c.c.$ having *branch points* at $\rho = e^{\pm i\Omega}/\alpha$; both the full view (a) and the detailed view (b) show that poles and zeros approach the branch point pairwise along a line that models the corresponding branch cut in the complex plane such that the complement of its domain of convergence has minimum capacity [42].

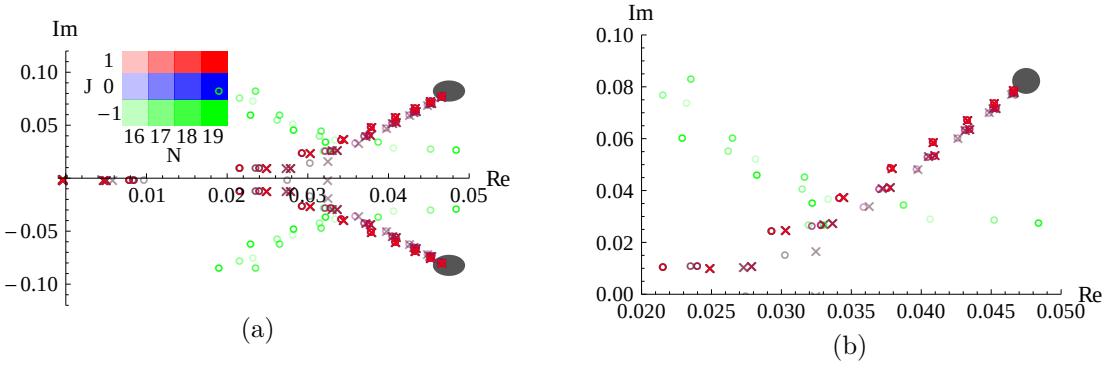

Fig. 28: Poles (×) and zeros (○) of the Padé approximants obtained from an expansion at infinity of $v(\rho) = \rho^{-7/3}\left(1 - \alpha e^{i\Omega}\rho\right)^{7/3} + c.c.$ having *branch points* at $\rho = e^{\pm i\Omega}/\alpha$ (and $\rho = 0$); as in the case of the expansions around the origin, both the full view (a) and the detailed view (b) show that poles and zeros approach the branch point pairwise along a line that models the corresponding branch cut.

they encircle the singularity with poles and zeros approaching it from opposite directions.

Lastly, we consider the case of branch points at these positions,

$$v(\rho) = \left(1 - \alpha e^{i\Omega}\rho\right)^{7/3} + c.c.\,, \tag{B.16}$$

where the exact form of the exponent is rather irrelevant; it does not affect the qualitative picture. Looking at Figure 27, this is obviously the pattern that reflects the one found for the average potential v best. There is a line of poles and zeros approaching the singular point. The fact that they come in pairs seems reasonably seeing as there is no real pole or zero along the line, so that they almost cancel each other. However, there is no exact match of poles and zeros, thus the defect is zero. It can be shown that this line outlines a branch cut related to the point in such a way that the region where the Padé approximants do not converge has minimum capacity [42].

Lastly, we would like to point out that Padé approximants calculated from series at different expansion points, namely infinity, show the same picture. Consider

$$v(\rho) = \rho^{-7/3}\left(1 - \alpha e^{i\Omega}\rho\right)^{7/3} + c.c.\,, \tag{B.17}$$

where we added the factor $\rho^{-7/3}$ in order that the leading order as $\rho \to \infty$ is zero; any integer value of the exponent would yield similar results. This function has branch points at the same locations as (B.16) plus the one at the origin. We expanded the function in a Taylor series at infinity and

calculated the Padé table as described in Section B.1.2. Examples of the distribution of poles and zeros of these approximants are shown in Figure 28.

The structure is very similar to the one obtained above for the expansion about the origin. It should be noted that the $J = -1$ approximant does not convey the information to the same extent because it is obviously unable to account for the correct leading order behavior (unless the coefficients b_N and b_{N-1} vanished, which is not the case). However, for all approximants with $J \geq 0$, the qualitative picture is the same as in the previous case. The branch cut, now winding towards the origin since the expansion point is at infinity, is sketched by a series of poles and zeros accumulating at the branch point. Interestingly, the branch point at the origin is highlighted much less than the other two. Presumably, this reflects the fact that it is located further away from the expansion point.

B.3 Padé-Hankel Method

The Padé-Hankel method provides a procedure to find in some sense optimum estimates for free parameters of a series expansion. It is based upon the idea of a two-point boundary value problem which is solved in terms of a series expansion at the first boundary. The solution can then be approximated using Padé functions again. Ideally, one can impose the boundary condition at the second point on the Padé expression itself. In general, this may not be possible, though, due to limited or slow convergence of the Padé approximants far away from the expansion point.

Therefore, a second procedure has been suggested by Fernández *et al.* [49] that amounts to enforcing a match of the series expansion and its Padé approximant to one more order. That is to say, the series and an $[M/N]$ approximant agree in the first $M+N+1$ terms by definition, but we require that the free parameter be chosen in such a way that the $(M+N+2)$-th terms match as well. The naïve hope is that this way the Padé expression reflects the function it is to approximate "better" at the remote boundary than before. Solving the corresponding equation for the free parameter for various orders of the approximation, one may find that the solutions indeed converge to its correct value. The good news is that this method has actually proven successful in many instances [15, 40, 49, 50].

Of course, the method can be carried out explicitly by computing the Padé approximant as shown above, re-expanding it into a Taylor series and comparing the $(M+N+2)$-th coefficients. The same result can be obtained more effectively, though, by requiring the vanishing of the *Hankel determinant* $\det H$ where the matrix H is related to $\bar{C}$ in (B.5) or (B.9), respectively [40].

Consider the case of a finite expansion point (Section B.1.1) first. There, $v(\rho)$ and $\mathcal{P}_{[M/N]}v(\rho)$ agree to order $\mathcal{O}\left(\rho^{M+N}\right)$. Requiring that this match extend to $\mathcal{O}\left(\rho^{M+N+1}\right)$ is equivalent to adding the case $i = M+N+1 = n_{\text{trunc}}+1$ to the second set of equations in (B.3). We can append this line to the matrix $\bar{C}$ and the inhomogeneity in (B.5), leading to an $(N+1) \times N$-matrix $\bar{C}'$, so that the resulting system of equations for the b_j becomes overdetermined.

As a general result of linear algebra, a system of equations like (B.5) is consistent if the coefficient matrix $\bar{C}$ and the matrix augmented by the inhomogeneity are of equal rank [51, pp. 232-233], i.e. the right-hand side depends linearly on the columns of the matrix $\bar{C}$. Seeing as it is useless to think about the Padé-Hankel method otherwise, we assume that the original Padé system, (B.5), has a unique solution, which means $\operatorname{rk} \bar{C} = N$. The extra line obtained from the Hankel condition cannot change this, and therefore $\operatorname{rk} \bar{C}' = N$, too. If this system is to be consistent, the augmented matrix

$$H_{ij} = c_{M+i-j+1} \qquad i, j = 0, \ldots, N \tag{B.18}$$

must have $\operatorname{rk} H = N$ as well. Here, we added the inhomogeneity before the first column of the matrix $\bar{C}'$ to obtain H (the extra minus sign does not change the argument). This condition is equivalent to the vanishing of the determinant of the $(N+1) \times (N+1)$ Hankel matrix H,

$$\det H = 0\,, \tag{B.19}$$

similar to [40].

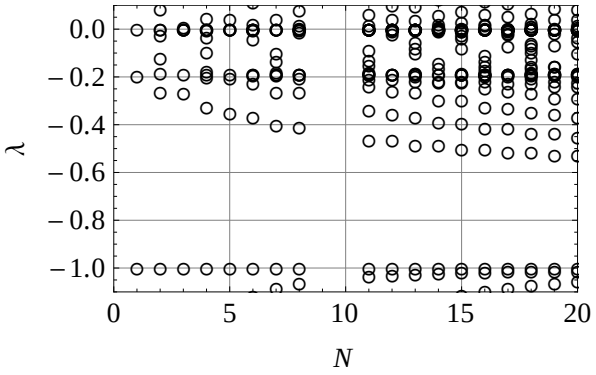

Fig. 29: Solutions λ of the Hankel condition in the interval $[-1, 0]$ for the $[N+3/N]$ approximants in the range $N = 1 \ldots 20$. The values $\lambda = 0, -1$ are under-represented. For unknown reasons, the computation failed at orders $N = 9, 10$.

We shall show now that this indeed works as a method to determine the correct value of the mass parameter λ of the small field series associated with the Wilson-Fisher fixed point. Nevertheless, it did not work, for instance, to find the correct guess of the constant A of the large field series.

In Figure 29 we plotted the values λ satisfying the Hankel condition for several approximants up to order [23/20]. We chose $M - N = 3$ again to reflect the correct large-field behavior. So as not to overload the diagram, we displayed every representative of the values $\lambda = 0$ and $\lambda = -1$ only once although numerous copies appear at every order. Furthermore, we excluded any complex-valued solutions, but the limitation to the interval $[-1, 0]$ is natural because there do not appear any converging roots outside this interval up to this order.

Inside the interval, by contrast, there is an accumulation at the prominent value of $\lambda \approx -0.186$. More precisely, $\lambda_\star = -0.186\,064\,249\,4\ldots$ is suggested to this order, in agreement with previous findings. This estimate makes use of the coefficients c_0 through c_{45}. For comparison, note that our first guess, obtained in Section 2.1.2 by an investigation of the roots of the c_n, was $\lambda_\star = -0.186\,064\,2\ldots$, and it included terms up to order 200.

It is straightforward to formulate the same condition for an expansion at infinity. Requiring a match in the next order coefficient is equivalent to enforcing the second part of (B.8) for $i = -(N+1)$ as well. Therefore, we add the corresponding line to the matrix $\bar{C}$ in (B.9), thus making the system overdetermined as before. In complete analogy to the previous case, we move the inhomogeneity on the right-hand side to the left, which leaves us with the Hankel matrix

$$H_{ij} = C_{-i-j-1}\,, \qquad i, j = 0, \ldots, N\,. \tag{B.20}$$

For the system to have a solution, we must have $\det H = 0$ again, and this provides a way to estimate an unknown parameter that the C_k depend on. By this way, we tried to compute critical exponents from the large field series in Section 3.4.

C Conversion to Units of Reference [43]

We derive the conversion between the units employed in this thesis and those of Bridle, Dietz, and Morris in [43], to which results of Section 2.1 are partly compared. All variables are defined as in Section 2.1 of this work; corresponding quantities in [43] will be denoted by a tilde. The fundamental classical fields are the same: $\phi = \tilde{\phi}$.

In this thesis, the effective potential v is expressed in terms of $\rho = \frac{1}{2}k^{2-d}\phi^2$ whereas in [43], $\tilde{v}$ is a function of $\tilde{\sigma} = \alpha k^{(2-d)/2}\phi$, where α is a (k-independent) scaling factor to be determined by

comparison of the resulting equation—its value is not given in the reference. Comparing in terms of the classical field ϕ, we find

$$\rho = \frac{1}{2\alpha^2}\tilde{\sigma}^2\,. \tag{C.1}$$

Furthermore, an additional constant $1/B$ is absorbed by the potential in $\tilde{v}$, such that we obtain the relation

$$v(\rho) = \frac{1}{B}\tilde{v}(\tilde{\sigma}) = \frac{1}{B}\tilde{v}(\alpha\sqrt{2\rho})\,. \tag{C.2}$$

From this it follows that $v'(\rho) = \alpha\tilde{v}(\tilde{\sigma})/B\tilde{\sigma}$ and $v''(\rho) = \alpha^2\tilde{v}''(\tilde{\sigma})/B\tilde{\sigma}^2 - \tilde{v}'/B\tilde{\sigma}^3$. Substituting into (2.1) leads to

$$\frac{6\pi^2}{B}3\tilde{v} - \frac{6\pi^2}{B}\frac{1}{2}\tilde{\sigma}\tilde{v} = \frac{1}{1+\frac{\alpha^2}{B}\tilde{v}''}\,,$$

which should be compared to the 3-dimensional fixed point equation (2.12) in [43]:

$$3\tilde{v} - \frac{1}{2}\tilde{\sigma}\tilde{v}' = \frac{1}{1+\tilde{v}''}\,. \qquad \text{(2.12) in [43]}$$

Thus we find $B = 6\pi^2$ and $\alpha = \sqrt{B} = \sqrt{6\pi^2}$, i.e.

$$\rho = \frac{1}{12\pi^2}\tilde{\sigma}^2\,, \qquad v(\rho) = \frac{1}{6\pi^2}\tilde{v}(\tilde{\sigma})\,. \tag{C.3}$$

Finally, comparing terms of power series such that

$$C_n\rho^n \stackrel{!}{=} \frac{1}{B}\tilde{C}_{2n}\tilde{\sigma}^{2n}$$

we find

$$C_n = \frac{(12\pi^2)^n}{6\pi^2}\tilde{C}_{2n} = 2(12\pi^2)^{n-1}\tilde{C}_{2n}\,. \tag{C.4}$$

In particular, $A = C_3 = 288\pi^4\tilde{A} = 28.054$ for the Wilson-Fisher fixed point (cf. (2.15) in [43]).

D Spectrum of Padé β Functions

In the following table, we present the spectra of various two-point Padé approximants for different weights (r, R) of the small and large field series. Calculations were performed using the method described in Sections 3.3 and 3.5. Please also note the annotations to the different abbreviations below.

Tab. 3: Spectrum of two-point Padé approximants for various orders and weights calculated from weighted flows (with $\beta_{r-1} \equiv 0$)[1]

M	**N**	**r**	**R**	$\Delta_{(\mathbf{0},\infty)}$[2]	**spectrum**	**NB** [3]
4	1	6	0	∞	-3, -1.550, 0, 1.162, 9.530,3.457[1]	
4	1	5	1	(∞)	-3, -1.537, 0, 0, 2.168, 1.648[1]	
4	1	4	2	(∞)	-3, -1.450, -1, 0, 0,4.851	
4	1	3	3	> 2	-3, -2, -1.085, -1, 0, 0	
4	1	2	4	1.0^{-2}	-3, -3, -2, -1, 0, 0	
4	1	0	6	1.3^{-3}	-5, -4, -3, -2, -1, 0	

– Continuing on next page –

– Tab. 3 (cont.) –

M	**N**	**r**	**R**	$\Delta_{(\mathbf{0},\infty)}{}^{2}$	**spectrum**	**NB** [3]
5	2	8	0	∞	-3, -1.539, 0, 5.989^{-1},4.683, 1.542^{1}, 3.932^{1}, 9.172^{1}	
5	2	7	1	(∞)	-3, -1.544, 0, 0, 7.399^{-1}, 6.400, 2.171^{1}, 5.955^{1}	
5	2	6	2	(∞)	-3, -1.550, -1, 0, 0, 1.162,9.530, 3.457^{1}	
5	2	5	3	(∞)	-3, -2, -1.537, -1, 0, 0, 2.168,1.648^{1}	
5	2	4	4	7.7^{-3}	-3, -3, -2,-1.450, -1, 0,0, 4.851	
5	2	3	5	3.1^{-4}	$-4, -3, -3, -2, -1.086, -1, 0, 0$	
5	2	2	6	1.4^{-4}	-5, -4, -3, -3,-2, -1, 0, 0	
5	2	1	7	1.6^{-4}	-6, -5, -4, -3,-2, -1, 0, 0	
5	2	0	8	1.1^{-4}	-7, -6, -5, -4, -3, -2, -1, 0	
6	3	10	0	∞	-3, -1.538, 0, 6.438^{-1}, 3.183, 9.208, 2.242^{1}, 4.734^{1}, 9.247^{1}, 1.784^{2}	
6	3	9	1	∞	-3, -1.537, 0, 0, 5.985^{-1}, 3.697,1.166^{1}, 2.890^{1}, 6.280^{1}, 1.312^{2}	
6	3	8	2	(∞)	-3, -1.539, -1, 0, 0,5.989^{-1}, 4.683, 1.542^{1}, 3.932^{1}, 9.172^{1}	
6	3	7	3	> 6	-4.026^{2}, -3, -1.544, -1.000, 0,0, 7.429^{-1}, 6.409, 2.204^{1},6.229^{1}	(N1)
6	3	6	4	2.7^{-4}	-3, -2, -1.579, -1,-2.478^{-1}, 0, 1.461, 9.732, 2.776^{1},1.711^{3}	(N1)
6	3	5	5	2.7^{-4}	-4, -3, -3, -2, -1.537, -1, 0, 0, 2.168, 1.648^{1}	
6	3	4	6	4.8^{-5}	-5, -4, -3, -3, -2, -1.450, -1, 0, 0, 4.851	
6	3	3	7	3.1^{-5}	-6, -5, -4, -3,-3, -2, -1.085, -1, 0,0	(N4)
6	3	2	8	4.3^{-5}	-7, -6, -5, -4, -3, -3, -2, -1, 0, 0	
6	3	1	9		Padé system of equations not solvable.	U
6	3	0	10	1.1^{-4}	-9, -8, -7, -6, -5, -4, -3, -2, -1, 0	
7	4	12	0	∞	-3, -1.539, 0, 6.712^{-1}, 3.061, 6.429, 1.479^{1}, 3.051^{1}, 5.713^{1}, 1.005^{2}, 1.713^{2}, 2.958^{2}	
7	4	8	4	4.5^{-3}	-3, -3, -2, -1.539,-1, 0, 0, 5.989^{-1},4.683, 1.542^{1}, 3.932^{1}, 9.172^{1}	
7	4	7	5	3.3^{-4}	-7.546^{1}, -3, -2.983, -2, -1.964, -1.616, -1, 0, 1.030 ± 9.653i, 7.133, 1.533^{2}	N1, C
7	4	6	6	3.5^{-5}	-5, -4, -3, -3,-2, -1.550, -1, 0, 0, 1.162, 9.530, 3.457^{1}	R
7	4	5	7	1.1^{-5}	-3.204^{1}, -9.824 ± 5.366i, -4.807, -3.647, -2.348, 1.609, 6.449 ± 2.353i, 1.464^{1}, 3.041^{1}, 5.403^{1}	R, C
7	4	4	8	9.3^{-6}	-7, -6, -5, -4, -3, -3, -2, -1.450, -1, 0, 0, 4.851	
7	4	3	9	4.8^{-3}	-2.447^{17}, -1.109^{17}, -3.232^{16}, -7.965^{1}, -2.093^{1}, -4.3972 ± 7.049^{1}i, 4.179^{1}, 1.504^{2}, 6.147^{2}, $6.881^{15} \pm 3.396^{17}$i	N11, C
7	4	0	12	4.9^{-3}	-11, -10, -9, -8, -7, -6, -5, -4, -3, -2, -1, 0	
8	5	14	0	∞	-3, -1.539, 0, 6.504^{-1}, 3.259, 5.577, 1.063^{1}, 2.146^{1}, 3.969^{1}, 6.831^{1}, 1.117^{2}, 1.771^{2}, 2.775^{2}, 4.448^{2}	
8	5	0	14	1.9^{-2}	-13, -12, -11, -10, -9, -8, -7, -6, -5, -4, -3, -2, -1, 0	

Annotations:

[1] The notation a^b is a shorthand for $a \times 10^b$. Decimal numbers are truncated, not rounded.

[2] Approximants marked with '∞' have infinite deviation determinable from analytic criteria, i.e. they exhibit poles on the positive real line or the wrong large-field behavior. For those marked with '(∞)', our numerical integration procedure does not converge, but they do show the correct behavior in the limit $\rho \to \infty$ (namely $v \sim A_\star \rho^3$).

[3] Codes:

- C Spectrum contains complex eigenvalues. Usually, these are the result of numerical instabilities in the flow calculation (code 'N') or limited computing resources (code 'R').
- N Numerical instabilities leading to indeterminancies in the calculation of the Padé coefficients' flow $\hat{\beta}_m$; the postpositioned figure indicates the number of affected terms. If the code is enclosed in parentheses, these difficulties could be overcome by iterating *Mathematica*'s symbolic simplification procedure before inserting numerical values for the terms in question.
- R Due to limited computing resources, the Padé coefficients' flows could not be evaluated with high-enough precision so as to verify that they vanish.
- U Padé approximant is undefined because the system of equations to calculate the Padé coefficients from the series coefficients is not solvable.

References

[1] Tomonaga, S. *On a Relativistically Invariant Formulation of the Quantum Theory of Wave Fields.* Prog. Theor. Phys. **1**, 27–42 (1946).

[2] Schwinger, J. *Quantum Electrodynamics. I. A Covariant Formulation.* Phys. Rev. **74**, 1439 (1948).

[3] Feynman, R. P. *The Theory of Positrons.* Phys. Rev. **76**, 749 (1949).

[4] Feynman, R. P. *Space-Time Approach to Quantum Electrodynamics.* Phys. Rev. **76**, 769 (1949).

[5] Wilson, K. G. *The renormalization group: Critical phenomena and the Kondo problem.* Rev. Mod. Phys. **47**, 773 (1975).

[6] Polchinski, J. *Renormalization and effective lagrangians.* Nucl. Phys. B **231**, 269–295 (1984).

[7] Morris, T. R. *The Exact Renormalisation Group and Approximate Solutions.* Int. J. Mod. Phys. **A9**, 2411–2450 (1994). arXiv:hep-ph/9308265v3.

[8] Wetterich, C. *Exact evolution equation for the effective potential.* Phys. Lett. B **301**, 90–94 (1993).

[9] Lavis, D. A and Bell, G. M. *Statistical Mechancis of Lattice Systems Volume 2.* Springer, (1999).

[10] Tetradis, N and Wetterich, C. *Critical exponents from the effective average action.* Nucl. Phys. B **422**, 541–592 (1994).

[11] Litim, D and Tetradis, N. *Approximate solutions of exact renormalization group equations.* OUTP-94-17P, HD-THEP-94-29 (1995). arXiv:hep-th/9501042v3.

[12] Bervillier, C., Boisseau, B., and Giacomini, H. *Analytical approximation schemes for solving exact renormalization group equations.* Nucl. Phys. B **789**, 525–551 (2008).

[13] Bervillier, C., Boisseau, B., and Giacomini, H. *Analytical approximation schemes for solving exact renormalization group equations. II Conformal mappings.* Nucl. Phys. B **801**, 296–315 (2008).

[14] Baker, G. A. *Application of the Padé Approximant Method to the Investigation of Some Magnetic Properties of the Ising Model.* Phys. Rev. **124**, 768 (1961).

[15] Abbasbandy, S and Bervillier, C. *Analytic continuation of Taylor series and the two-point boundary value problems of some nonlinear ordinary differential equations.* Appl. Math. Comput. **218**, 2178 (2011).

[16] Peskin, M. E and Schroeder, D. V. *An Introduction to Quantum Field Theory.* Westview Press, first edition (1995).

[17] Gies, H. *Introduction to the functional RG and applications to gauge theories.* (2006). arXiv:hep-ph/0611146v1.

[18] Berges, J., Tetradis, N., and Wetterich, C. *Non-Perturbative Renormalization Flow in Quantum Field Theory and Statistical Physics.* Phys. Rept. **363**, 223–386 (2002). arXiv:hep-ph/0005122v1.

[19] Delamotte, B. *An introduction to the Nonperturbative Renormalization Group.* (2007). arXiv:cond-mat/0702365v1.

[20] Rosten, O. J. *Fundamentals of the Exact Renormalization Group.* Phys. Rep. **511**, 177–272 (2012). arXiv:1003.1366v4.

[21] Litim, D. F. *Optimized Renormalization Group Flows.* Phys. Rev. **D64**, 105007 (2001). arXiv:hep-th/0103195v2.

[22] Zumbach, G. *The renormalization group in the local potential approximation and its applications to the O(n) model.* Nucl. Phys. B **413**, 754–770 (1994).

[23] Litim, D. F. *Derivative expansion and renormalization group flows.* JHEP **0111**, 059 (2001). arXiv:hep-th/0111159v1.

[24] Harvey-Fros, C. S. F. *The local potential approximation of the renormalization group.* Ph.D. thesis, University of Southampton (1999). arXiv:hep-th/0108018v1.

[25] Morris, T. R. *Equivalence of Local Potential Approximations.* JHEP **0507** (2005). arXiv:hep-th/0503161v3.

[26] Litim, D. F. *Critical exponents from optimised renormalization group flows.* Nucl. Phys. B **631**, 128–158 (2002). arXiv:hep-ph/0203006v2.

[27] Zinn-Justin, J. *Quantum Field Theory and Critical Phenomena.* Oxford University Press, third edition (1996).

[28] Wipf, A. *Statistical Approach to Quantum Field Theory.* Springer, first edition (2013).

[29] Königsberger, K. *Analysis 1.* Springer, sixth, revised edition (2004).

[30] Codello, A. *Scaling Solutions in Continuous Dimension.* J. Phys. A: Math. Theor. **45** (2012). arXiv:1204.3877v2.

[31] Gneiting, C. *Higgs mass bounds from renormalization flow.* Diploma thesis, Heidelberg University (2005).

[32] Popov, V. S., Eletskii, V. L., and Turbiner, A. V. *Higher orders of perturbation theory and summation of series in quantum mechanics and field theory.* Zh. Eksp. Teor. Fiz. **74**, 445–465 (1978).

[33] Fischer, J. *On the role of power expansions in quantum field theory.* Int. J. Mod. Phys. **A12**, 3625–3663 (1997). arXiv:hep-ph/9704351v1.

[34] Königsberger, K. *Analysis 2.* Springer, fifth, corrected edition (2004).

[35] Bender, C. M and Orszag, S. A. *Advanced Mathematical Methods for Scientists and Engineers.* Springer, first edition (1999).

[36] Baker, G. A and Graves-Morris, P. R. *Padé Approximants.* Cambridge University Press, second edition (1996).

[37] Hunter, D. L and Baker, G. A. J. *Methods of Series Analysis. I. Comparison of Current Methods Used in the Theory of Critical Phenomena.* Phys. Rev. B **7**, 3346 (1973).

[38] Yamada, H. S and Ikeda, K. S. *A Numerical Test of Pade Approximation for Some Functions with singularity.* (2014). arXiv:1308.4453vs.

[39] Van Assche, W. *Pade and Hermite-Pade approximation and orthogonality.* Surveys in Approximation Theory **2**, 61–91 (2006). arXiv:math/0609094v1.

[40] Amore, P and Fernandez, F. M. *Rational Approximation for Two-Point Boundary value problems.* (2007). arXiv:0705.3862v1.

[41] Cuyt, A and Wuytack, L. *Nonlinear methods in numerical analysis.* Elsevier Science Publishers B.V., first edition (1987).

[42] Stahl, H. *The Convergence of Padé Approximants to Functions with Branch Points.* Journal of Approximation Theory **91**, 139–204 (1997).

[43] Bridle, I. H., Dietz, J. A., and Morris, T. R. *The local potential approximation in the background field formalism.* JHEP **1403**, 93 (2014). arXiv:1312.2846v2.

[44] Private communication with Julia Borchardt, Theoretisch-Physikalisches Institut, Friedrich-Schiller-Universität Jena.

[45] Pelissetto, A and Vicari, E. *Critical Phenomena and Renormalization-Group Theory.* Phys. Rept. **368**, 549–727 (2002). arXiv:cond-mat/0012164v6.

[46] Guida, R and Zinn-Justin, J. *Critical Exponents of the N-vector model.* J. Phys. **A31**, 8103–8121 (1998). arXiv:cond-mat/9803240v3.

[47] Ferrenberg, A. M and Landau, D. P. *Critical behavior of the three-dimensional Ising model: A high-resolution Monte-Carlo study.* Phys. Rev. **B44**, 5081–5091 (1991).

[48] Bervillier, C., Juttner, A., and Litim, D. F. *High-accuracy scaling exponents in the local potential approximation.* Nucl. Phys. B **783**, 213–226 (2007). arXiv:hep-th/0701172v2.

[49] Fernández, F. M., Ma, Q., and Tipping, R. H. *Tight upper and lower bounds for energy eigenvalues of the Schrödinger equation.* Phys. Rev. A **39**, 1605 (1989).

[50] Abbasbandy, S and Hayat, T. *Solution of the MHD Falkner-Skan flow by Hankel-Padé method.* Phys. Lett. A **373**, 731–734 (2009).

[51] Fischer, G. *Lehrbuch Lineare Algebra und Analytische Geometrie.* Springer, second edition (2012).